GAMMA BACKGROUND STUDIES FOR THE XENON EXPERIMENT USING A HIGH PURITY GERMANIUM DETECTOR

By

JESSE ISAAC ANGLE

A DISSERTATION PRESENTED TO THE GRADUATE SCHOOL
OF THE UNIVERSITY OF FLORIDA IN PARTIAL FULFILLMENT
OF THE REQUIREMENTS FOR THE DEGREE OF
DOCTOR OF PHILOSOPHY

UNIVERSITY OF FLORIDA

2008

To everyone who stood by me when times got rough.

ACKNOWLEDGMENTS

I would like to thank my advisor Laura Baudis (currently at the University of Zurich) for providing me with the opportunity to work on such an exciting and cutting-edge experiment. I would like to express my gratitude to all of my fellow graduate students at the University of Florida for helping me to maintain my sanity through this thing we call graduate school. And lastly I would like to thank my wife Wendi Angle for standing by me and helping me to get where I am.

TABLE OF CONTENTS

LIST OF TABLES

LIST OF FIGURES

Abstract of Dissertation Presented to the Graduate School
of the University of Florida in Partial Fulfillment of the
Requirements for the Degree of Doctor of Philosophy

GAMMA BACKGROUND STUDIES FOR THE XENON EXPERIMENT USING A HIGH PURITY GERMANIUM DETECTOR

By

Jesse Isaac Angle

May 2008

Chair: John Yelton
Major: Physics

The XENON Dark Matter Experiment, deployed at the Gran Sasso National Laboratory in Italy on March 2006, is a liquid noble gas detector designed to directly detect dark matter. The detector uses a dual-phase (gas/liquid) Xenon target to search for nuclear recoils associated with nucleus-WIMP interactions. Due to the high sensitivity needed in such an experiment, it is vital to not only reduce the background but to also understand the remaining background so as to aid in the understanding of the data as well as to facilitate upgrades beyond the early Research and Development phases.

Many of the components of the XENON10 detector have been screened using a High Purity Germanium Detector known as the GATOR detector. Full analysis of the screening data requires Monte Carlo simulations of the GATOR detector and the sample. Results from this screening will be presented. Using the information obtained from the screening operation, Monte Carlo simulations of the XENON10 electron recoil background will be examined and compared to the actual detector data. The success of this simulation to data comparison indicates that we have a good understanding of the XENON10 gamma background and will be able to make more informed decisions regarding the next stage of detector development. This type of analysis has aided in the selection and design of many of the materials and components being incorporated into the new XENON100 detector, the next generation detector which will be capable of improving the limit set by XENON10 by at least an order of magnitude.

CHAPTER 1
INTRODUCTION

1.1 Overview

This thesis will attempt to summarize my work within the University of Florida (UF) group of the XENON collaboration over the last three and a half years. This chapter will offer a brief introduction to dark matter and the ongoing search for it. Section 1.2, will be devoted to a brief historical overview of dark matter in general and the evidence for its existence. Section 1.3 will go into some of the physical attributes of dark matter, section 1.4 will overview some of the detection methods being used in the hunt for dark matter and section 1.5 will detail some of the specifics of the XENON experiment.

Chapter 2 is devoted to the GATOR detector, the solid-state high purity Germanium crystal detector that was used to perform most of the measurements detailed herein. Section 2.1 provides an overview of GATOR and its operation in the Soudan Low Background Counting Facility (SOLO). Sections 2.2 through 2.6 discuss the GATOR background through various rebuilds. Sections 2.7 and 2.8 briefly covers several failures the GATOR detector experienced whilst installed at SOLO. These background analysis and calculations as well as the analysis regarding the detector interruptions were completed by me.

Chapter 3 will be centered around the material screening for which the GATOR detector was designed. The first section will summarize the analysis procedures I used for analyzing the screening data, followed by a section summarizing all of these results. Each material I screened will be given it's own section following that.

Chapter 4 will apply the screening results to the XENON10 detector. Section 4.1 will be devoted to the specifics of the XENON10 detector while section 4.2 will detail the individual analysis I completed for the various components. Section 4.3 will go into the work done on the full XENON10 background simulations.

Chapter 5 contains all of the other work I accomplished for the XENON collaboration abroad and at UF. Section 5.1 focuses on the XENON prototype built at UF. Section 5.2 details the gas system constructed at UF for said prototype and section 5.3 will discuss the electric field simulations done for the UF Prototype Inner Detector.

1.2 Evidence for Dark Matter

The existence of dark matter was first hypothesized by Swiss astrophysicist Fritz Zwicky working at Caltech in 1933. The "missing mass problem", as it became known, was discovered when Zwicky estimated the mass of the Coma cluster using two different techniques. By comparing the mass as determined by the motion of galaxies in the cluster to the mass obtained by looking at the number of galaxies and the brightness of the cluster, Zwicky found that the Coma cluster contained approximately 400 times as much mass as would be expected from just the visible matter. Zwicky hypothesized that some sort of invisible matter (what we now refer to as dark matter) must be present for the Coma cluster to behave as observed [1–3].

It wasn't until almost 40 years later when corroborating evidence for Zwicky's missing mass was found. Vera Rubin, working at the Department of Terrestrial Magnetism at the Carnegie Institution of Washington measured the rotational velocities of stars within edge on spiral galaxies to a higher degree of precision than had ever been done before. Her results, first presented at a meeting of the American Astronomical Society in 1975, show that at higher radii the velocity of stars is relatively flat even at large distances instead of the declining velocity curve that had been predicted[4]. See Figure 1-1 for an example of this behavior. Rotation curves of this kind are often considered the most common example for dark matter's existence[5]. Even though these results were originally met with skepticism, more data kept coming in that agreed with this hypothesis. One of the typical attempts to explain this missing mass resulted in the proposal that a large portion of the mass in a galaxy is stored within a halo of Zwicky's dark matter. While the original measurements that led to the "discovery" of dark matter are based around the motion

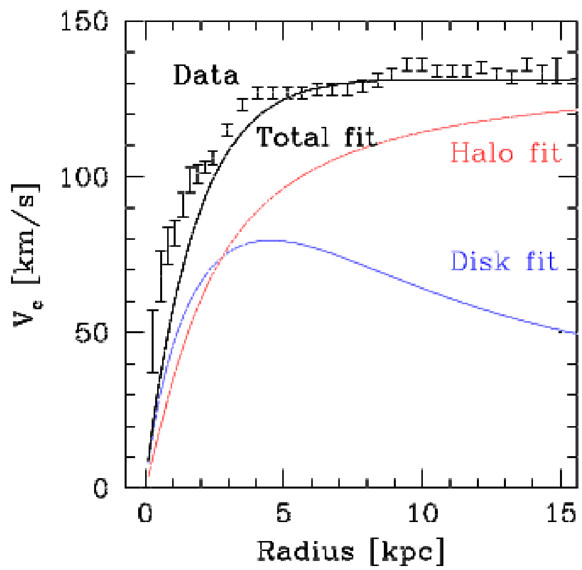

Figure 1-1. Velocity curve for the nearby spiral galaxy NGC2403. The blue line is the behavior one would expect from a $1/r^2$ decline. The red is the supposed dark matter halo that is needed to combine with the disk fit in order to match the data, shown in black. Image courtesy of http://burro.cwru.edu/JavaLab/RotcurveWeb/main_BACK.html.

of stars within galaxies and galaxies within clusters, other types of measurements also postulate the existence of some sort of dark matter.

Studies of the Cosmic Microwave Background (CMB) provide an accurate means of probing cosmological parameters. Data from the Wilkinson Microwave Anisotropy Probe (WMAP) alone is able to put constraints on both the matter content in the universe as well as the baryonic content in the universe[6–8].

$$\Omega_b h^2 = 0.024 \pm 0.001 \tag{1–1}$$

$$\Omega_M h^2 = 0.14 \pm 0.02 \tag{1–2}$$

The value Ω is the matter density of a substance averaged across the Universe in relation to the critical density, that density for which the Universe would be Euclidean, or flat (see Equation 1–3). Ω_M is the density of all gravitation matter while Ω_b is the density of baryonic matter. h represents the uncertainty in the Hubble Constant ($H_o = 100 \cdot h \cdot$

km^2s^{-1}) and takes on values ranging from 0.4 to 1.

$$\Omega_X = \frac{\rho_X}{\rho_{critical}} \tag{1–3}$$

This value for the baryonic content in the universe is in agreement with that as determined by Big Bang Nucleosynthesis. To agree with the measured abundances of light elements, namely helium, lithium and deuterium, the baryonic content must be in the following range:

$$0.018 < \Omega_b h^2 < 0.023 \tag{1–4}$$

These numbers strongly indicate that the majority of matter in the universe is non-baryonic and poorly understood. Note that the Ω variable represents the ratio of the density of the substance in discussion to the critical density, that density for which the universe is flat. WMAP measurements further indicate that the universe is flat and Ω_{total} is equal to unity. This implies additionally that dark matter and baryonic matter make up only a small portion of the total density in the universe.

In 2006, the National Aeronautics and Space Administration (NASA) published evidence for what they termed "direct proof of dark matter". A team led by Doug Clowe of the University of Arizona at Tucson spent over 100 hours observing the galaxy cluster 1E0657-56 with the Chandra Telescope. The x-ray image produced with this telescope gives an idea of the distribution of mass due to ordinary baryonic matter, believed to be mostly hot gas within the cluster. Gravitational lensing done with the Hubble Space Telescope, the European Southern Observatory's Very Large Telescope and the Magellan optical telescopes provide a measurement of the distribution of total mass within the cluster due to ordinary matter as well as dark matter. It seems quite clear that the total mass and the mass due to regular matter are drastically different. The ordinary matter appears to have experienced drag forces during a past collision with a smaller cluster. The dark matter did not experience such a drag force since it is largely collisionless and thus became separated from the regular matter. This is shown in the data by a significant separation between the location of the ordinary matter and the total mass of the cluster. See Figure 1-2[9]. Dark matter's existence is also a big aid to those who study structure

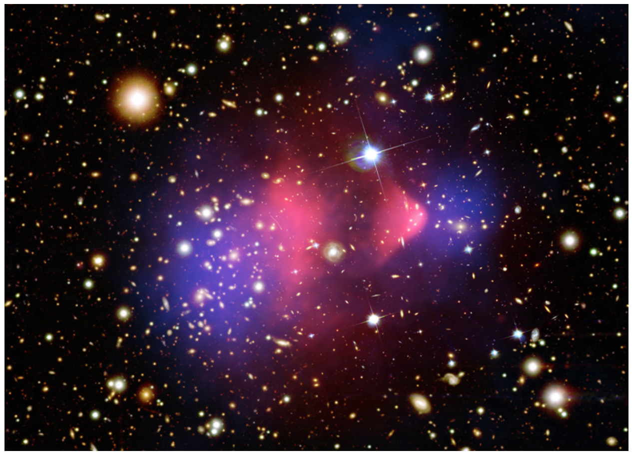

Figure 1-2. Composite image of cluster 1E0657-56. The red x-ray image represents the location of the majority of the regular matter (hot gas in this case) within the cluster. The blue, taken from gravitational lensing, represents the total mass within the cluster, strongly indicating the presence of dark matter separated from the regular matter. Image courtesy of http://chandra.harvard.edu/photo/2006/1e0657/.

formation, where the inclusion of dark matter into some of the theories provides very accurate results that compare quite well to observations of the current structure of the universe. Numerous N-body simulations seeking to replicate the observed structures have met with remarkable success integrating dark matter into the simulations. Figure 1-3 is one example of such an N-body simulation[10–12]. Measurements taken from intracluster gas within clusters and interstellar gas at the edges of galaxies indicate that dark matter makes up roughly 95 percent of all gravitating matter. Gravitational lensing can provide a density profile of dark matter within clusters and has led to the discovery of what is believed to be dark matter galaxies[13, 14].

1.3 Composition of Dark Matter

One theory of dark matter proposed that the major component of the unseen mass was composed of Massive Compact Halo Objects (MACHOs). Included in this category are brown dwarfs, white dwarfs, neutron stars and black holes. All are massive objects

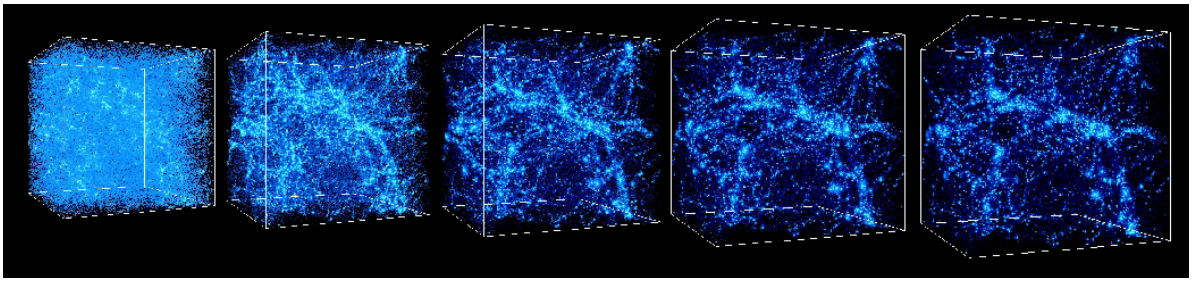

Figure 1-3. Example of the progress of a typical N-body simulation. The images here represent evolution of structure within a 140 million light year box from a redshift of 30 to a redshift of 0. Image courtesy of http://cosmicweb.uchicago.edu/index.html.

which are very difficult to detect through normal observational techniques, making them a possible dark matter candidate[15]. Unfortunately, it is believed that a high production rate of any of these objects would have observable side effects that we do not see (the amount of baryons needed would change the elemental abundances, especially deuterium)[16]. The EROS-2 project observed the Magellanic Clouds for microlensing events, looking for stars gaining brightness as a MACHO passed in front of it via gravitational lensing. Their findings indicate that MACHOs can make up approximately only 8% of the Milky Way's dark matter halo[17]. So while a small percentage of dark matter may be composed of MACHOs, the main component is likely composed of something more complicated.

On the extreme other end of the mass scale, weighing between 10^{-6} and 10^{-2} eV is the axion. The axion's existence was postulated in 1977 by Roberto Peccei and Helen Quinn to solve the strong CP problem of Quantum Chromodynamics (QCD). Such a particle would have a very small mass but if it existed its properties would be inline with the expected properties of dark matter. Detection schemes for axions are vastly different than those for other dark matter candidates. Resonant microwave cavities are used to attempt to enhance the axions coupling to the electromagnetic field. If the cavity's frequency is tuned to the axion mass a peak will be visible in the frequency spectrum. Experiments such as the Axion Dark Matter eXperiment (ADMX) are using such cavities to search for axions and place upper limits of the axion density in local discrete flows[18–20].

One of the most promising candidates for dark matter is the Weakly Interacting Massive Particle (WIMP). Such a particle would interact via the weak force, thus its name, and gravity but not the electromagnetic force, rendering them virtually invisible to normal detection. One of the more promising WIMP candidates is the neutralino. The promising theory of supersymmetry predicts that all Standard Model particles will have a supersymmetric partner with the same quantum number but with a spin that differs by 1/2. Since the super-partners to the photon, the Z boson and the neutral higgs (known as the photino, the zino and the higgsino respectively) all have the same quantum number, they can mix into different eigenstates of the mass operator to form four different neutralinos. In some Super-Symmetry models the lightest of the neutralinos, with a mass around 100 GeV to 1 TeV is called the lightest supersymmetric particle (LSP)[21, 22].

This LSP is believed to be stable, couple with other particles via the weak interaction, and some calculations show that it can be formed in the early universe in the correct abundance to account for the expected amount of dark matter today. Such an abundance in the early universe also helps to explain structure formation, in which the basic structures within the galaxy are initially created by a gravitational accumulation of dark matter with ordinary matter following later to form stars, galaxies and clusters. All in all a quite promising particle indeed. It is the neutralino which the XENON experiment is built to search for.

1.4 Methods of Dark Matter Detection

There are two basic schemes for detecting WIMP dark matter; indirect detection and direct detection. Indirect detection operates under the theory that in a dark matter - dark matter collision annihilation can occur, releasing particles that can create an observable signal. Indirect searches of this nature probe the galactic center and the center of the sun due to the possible accumulation of dark matter in these gravity wells. Many of the searches now operating are looking for the tell tale gamma ray signal, a mono energetic line with mean energy equal to that of the dark matter particle mass. It is believed that such experiments like the Very Energetic Radiation Imaging Telescope Array System (VERITAS) and the Gamma-ray Large Area Space Telescope (GLAST) will be able to search the entire range of energies where the neutralino is thought to reside, namely 30 GeV to 3 TeV[23].

In contrast, direct detection schemes rely on the assumption that dark matter is composed of WIMPs and thus can interact via the weak interaction allowing the WIMP to collide with the nucleus of the detector material. The two basic types of interactions that can occur are spin-independent and spin dependent. Spin dependent interactions occur when the spin of the WIMP couples with the spin of the nucleon. Spin independent interactions occur when the WIMP couples to the mass of the nucleon. It is believed that spin independent interactions dominate for nuclei with A>30, however searching for both types will be important to insuring detection of dark matter.

There are many different direct detection experiments using a wide variety of materials. The Cryogenic Dark Matter Search (CDMS) looks for a phonon signal within the Germanium and Silicon detectors. The Dark Matter (DAMA) collaboration found their controversial result using a Sodium Iodine detector that looked for photons. The XENON experiment uses liquid Xenon as its sensitive material.

1.5 The XENON Experiment

Figure 1-4 shows the results from a handful of the direct detection experiments throughout the world. CDMS-II's data from their Germanium - Silicon detectors, WARP's (Wimp ARgon Programme) data from their liquid argon detector, data from Edelweiss's germanium bolometers, and the limit from Zeplin's liquid Xenon detector are all shown with the current limit from XENON10's liquid xenon detector. All of these experiments operate under the same basic philosophy, trying to measure the interaction between a passing WIMP and the detector material[24]. The XENON experiment is a direct

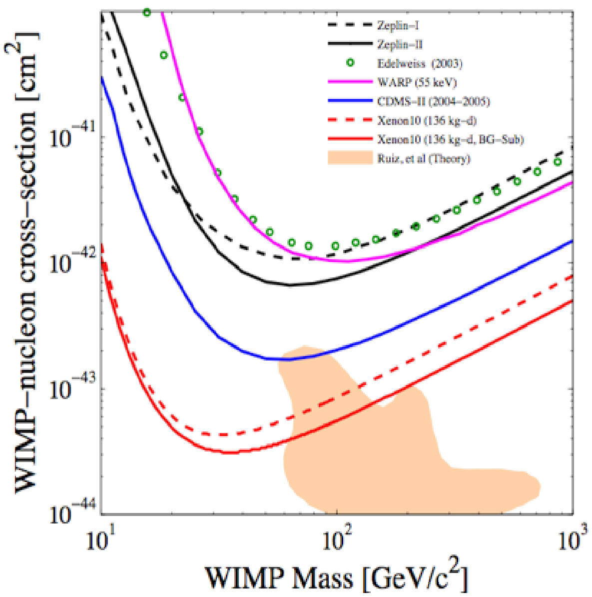

Figure 1-4. Dark matter limit plot showing the limits based on data from XENON10, CDMS-II, WARP, Edelweiss, Zeplin 1 and Zeplin 2 as well as one prediction by Ruiz et al. Image courtesy of http://xenon.astro.columbia.edu/.

detection experiment that plans to measure the interaction between a WIMP and a Xenon nucleus within the detector volume. However, other particles can also interact with Xenon making finding the WIMP signal not as straight forward as it originally sounds. Photons and electrons for instance interact via electronic recoil with the Xenon atoms creating a signal that can be and has to be separated from the nuclear recoil signal created by WIMPs and neutrons.

There are two primary interaction channels that occur in the liquid Xenon, ionization and excitation. Both channels begin with an electric or nuclear recoil and end with a 182 nm gamma ray being emitted[25].

Excitation

$$Xe + RECOIL \rightarrow Xe^*$$

$$Xe^* + Xe \rightarrow Xe_2^*$$

$$Xe_2^* \rightarrow 2Xe + GAMMA$$

Ionization

$$Xe + RECOIL \rightarrow Xe^{+} + e^{-}$$

$$Xe^{+} + Xe \rightarrow Xe_2^{+}$$

$$Xe_2^{+} + e^{-} \rightarrow Xe^{**} + Xe$$

$$Xe^{**} \rightarrow Xe^{*} + HEAT$$

$$Xe^{*} + Xe \rightarrow Xe_2^{*}$$

$$Xe_2^{*} \rightarrow 2Xe + GAMMA$$

The XENON detector is a dual phase (mostly liquid with a small gas layer) time projection chamber (TPC). When a Xenon atom undergoes a electronic or nuclear recoil, UV scintillation photons are released and collected by a photomultiplier tube (PMT) array via the above interaction channels. This signal is referred to as the primary light or S1. In the recoil, the ionization electrons that are released will drift upwards due to the high electric field placed on the liquid volume. When these electrons are extracted into the gas phase they are accelerated by a different electric field and will interact with the gaseous Xenon, creating a secondary signal referred to as proportional scintillation light or S2.

This setup provides us with information regarding the event with very little analysis. X and Y position can be determined based on the number of photons that strike individual PMTs. A simple center of mass calculation can determine the X and Y position within an accuracy of a few millimeters. Using the temporal separation between S1 and S2 as well as a knowledge of the drift velocity of electrons in liquid Xenon, the Z position of the event can be calculated to an accuracy of less than one millimeter. A good 3D localization allows multiple scatters to be eliminated as well as allowing fiducial volume cuts to be made.

One of the largest advantages to this particular TPC is its very strong ability to discriminate electron recoils from nuclear recoils. It has been shown earlier by the XENON collaboration that the number of electrons released in an electron recoil interaction is significantly higher than the number released in a nuclear recoil. Each type of recoil interaction will undergo different amounts of the two channels allowing simple discrimination. Thus comparing the S1 signal to the S2 signal can provide a means of discriminating many background events from the events of interest.

CHAPTER 2
GATOR DETECTOR

2.1 High Purity Germanium Detectors

Gamma ray spectroscopy is a very well established science so only a brief summary of high purity Germanium detectors towards this application will be discussed. The basic principle of gamma ray spectroscopy is to transfer the energy of the incident photon into something more detectable, electron-hole pairs in the case of a Germanium detector. As a photon enters the Germanium crystal its energy is transferred to the electrons via photoelectric absorption, compton scattering, and pair production[1] . One of the largest advantages to using a semiconductor detector is that the ionization energy, the energy required to release an electron to the conduction band, is very small, on the order of 3 eV. This means that an incident photon will be able to create many electron-hole pairs which enables semiconductor detectors to achieve a better energy resolution than other gamma ray detectors.

In order to manufacture crystals large enough to create an effective gamma ray detector, the current method is to reduce the level of impurities within the semiconductor crystal so as increase the depletion depth. Impurity levels on the order of 1 part in 10^{12} can be reached with Germanium, making it one of the most highly purified materials available at the commercial level. To reach these levels, first the stock material is purified by a technique referred to as zone refining. The material is heated locally and the heated regions are passed from one end of the crystal to the other. Since the impurities are more soluble in the molten Germanium, they are thus passed out of the crystal. This purified stock is then used to grow the crystal detectors.

[1] At the energies relevant for the XENON material screening, photoelectric absorption and compton scattering will be the dominant sources of energy transfer.

Once the crystal has been grown into whatever shape and size is desired, the main thing left is to modify the crystal so that the electric field can be applied. This is commonly done by doping the two surfaces that are to become the contacts (Lithium and Boron doping are quite common for this purpose). Doping the two surfaces can drastically increase the conductivity in that region of the crystal, making an ideal electrical contact. Applying a voltage across these two contacts around 3-5 kV is enough to reach the electric field value for electron drift velocity saturation. Cool the crystal with liquid nitrogen to reduce thermal current, apply the necessary voltage and we have got the basis for a very powerful gamma ray detector.[26]

2.2 Details of the GATOR Detector

Purchased from the Canberra Company, the GATOR detector consists primarily of a 2.2 kg high purity Germanium crystal installed as an ionization detector. The crystal is a p-type Germanium semiconductor crystal that was grown in a cylindrical orientation measuring 82 mm in diameter and 81.5 mm in height. The outer electrode comprised of Germanium doped with Lithium along the outer radial surface and the inner electrode comprised of Germanium doped with Boron along the surface of a 10.5 mm diameter, 67 mm deep hole in the center of the crystal provide the strong electric field (on the order of 1.65 keV/cm) along the crystal's radial axis. The crystal holder, cryostat and cold finger are all composed of ultra-low background Copper to minimize the intrinsic background of the detector. GATOR was installed inside a thick Lead shield (roughly 9" of newer Lead and 2" of ancient Lead) deep in the Soudan Underground Laboratory in Minnesota. It was initially installed into SOLO (Soudan Low Background Counting Facility), which was constructed by the XENON group at Brown and is currently operated by Brown.[2] The excellent energy resolution of this detector (approximately 1.89 keV at 1173 keV and 2.17

[2] For additional information about the SOLO facility, please see Brown's website at http://particleastro.brown.edu/SOLO/.

Figure 2-1. Outer Copper cryostat resting in the original Lead shield in the SOLO facility at the Soudan Underground Laboratory in Minnesota.

keV at 1332 keV) allow for the various decays present, usually ^{238}U, ^{232}Th, ^{40}K, ^{137}Cs and ^{60}Co,to be identified. It is mainly these five decays that will be searched for by GATOR in the various samples provided.

2.3 Pre Shield Rebuild: GATOR Background

Before sample analysis can be discussed, we must first examine the background intrinsic to the GATOR detector. The original GATOR background can be seen in Figure 2-2. In the background we can see low energy Pb x-rays (around 80 keV), the 511 keV electron - positron annihilation line, the 1460 keV ^{40}K line, and many lines from the ^{194}Au and ^{207}Bi decays, as well as the continuum from ^{210}Pb bremsstrahlung and compton scattering. The strong Gold and Bismuth lines visible were believed to originate from a single "hot spot" within one of the newer Lead bricks immediately next to the GATOR detector. One of our collaborators, Brown University again, had seen similar data before in their detector which was determined to come from a Lead brick that had been previously activated during an accelerator experiment. Under this assumption we can therefore calculate how much Lead is between the detector and the supposed hot spot. The lower energy lines will be attenuated more by the intervening Lead, so by comparing

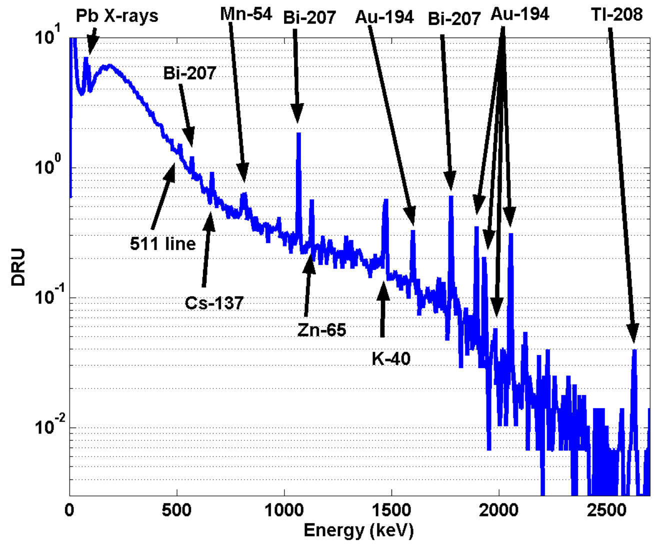

Figure 2-2. Original GATOR Background over a total of 44 kg days (2.2 kg crystal, 21.877 days), from 7-12-2005 to 8-3-2005. Many of the lines visible originate from ^{194}Au and ^{207}Bi indicating a strong localized contamination near the detector.

Table 2-1. Data selected to determine the location of the hot spot within the Lead shield.

Line Energy (keV)	Mass Atten. Coeff. (cm^2/g)	Amplitude (counts)	B.R.
Au Low Energy - 1468	0.0519	34.5	6.4%
Au High Energy - 2042	0.0459	24.8	3.6%
Bi Low Energy - 569	0.1361	33.7	97.74%
Bi High Energy - 1064	0.0679	172.1	74.5%

the heights of the low energy lines and the high energy lines to what we would expect allows us to determine the depth of Lead.

The National Institute of Standards and Technology (NIST - http://physics.nist.gov) provides tables and graphs of the photon mass attenuation coefficient for many elements and compounds, including elemental Lead. Branching ratios for the various lines visible are also readily available. Two lines from each decay (^{194}Au and ^{207}Bi) were chosen and the subsequent data found are summarized in Table 2-1 The intensity of radiation as a function of thickness is determined by Equation 2–1.

$$I = I_o e^{-MAC\cdot\rho\cdot x} \tag{2–1}$$

where I is the measured intensity, I_o is the emitted intensity, MAC is the mass attenuation coefficient, ρ is the material density and x is the thickness. Since we don't know the actual intensities, we must take the ratios using the number of counts for the measured intensities and the branching ratios for the emitted intensities as we know these ratios.

$$\frac{I_1}{I_2} = \frac{I_{o1} e^{-MAC_1 \cdot \rho \cdot x}}{I_{o2} e^{-MAC_2 \cdot \rho \cdot x}} \tag{2–2}$$

Solving for the thickness of Lead, x, yields

$$x = -ln(\frac{I_1 I_{o2}}{I_2 I_{o1}}) \frac{1}{\rho(MAC_1 - MAC_2)} \tag{2–3}$$

Placing the actual numbers into the equation (density of Lead = 11,340 kg/m^3) yields 3.60 cm of Lead as determined by the ^{194}Au lines and 2.50 cm as determined by the ^{207}Bi lines. The actual value is probably closer to 2.50 cm as 100% detector efficiency is assumed and attenuation due to any Copper in the path has been ignored. Regardless, given that the Lead bricks are 5 cm thick (a standard Lead brick in this shield is 2" x 4" x 8") next to the detector, the hot spot appears to be within one of the two newer bricks lying directly beside the detector.

2.4 Post Shield Rebuild: GATOR Background

With so much of the background coming from an activated brick right next to the GATOR detector, the SOLO shield was rebuilt around November 9th, 2005 in order to remove said brick. The newer Lead bricks next to the GATOR detector were replaced with older, lower radioactivity bricks. During this rebuild, approximately 140 bricks were found with markings indicating that they were used by the DOE prior to their inclusion in SOLO. These bricks, assumed to be of higher radioactivity than normal bricks, were replaced with non-DOE marked bricks. The background spectrum after the shield rebuild can be seen in Figure 2-3. After the rebuild, the observed background was much lower, reduced from 200 total counts per hour to 63 total counts per hour (integrated from roughly 30 keV to 2550 keV, which is almost the entire spectrum range). Figure 2-4

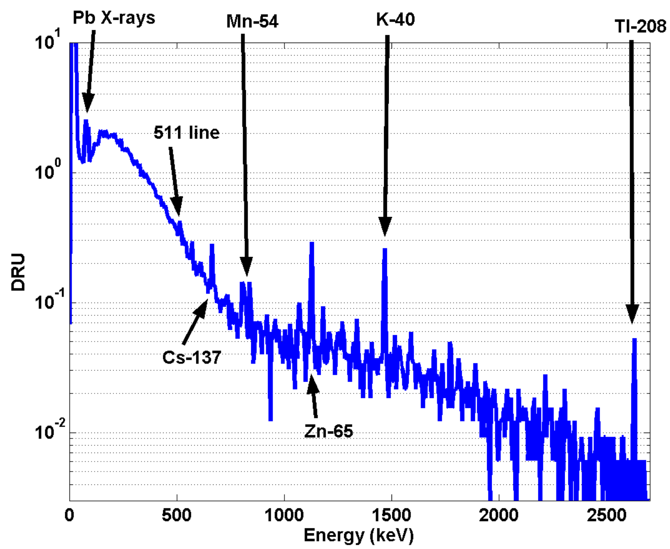

Figure 2-3. New GATOR Background. The above background was taken over 57 kg days from 11-11-2005 to 12-8-2005. It is clear that the background is improved, simply noting the reduced number of visible lines.

directly compares the two background spectrum (post and pre shield rebuild) after rescaling them both to DRU (events / kg / day / keV). The many Gold and Bismuth lines were no longer seen as well, indicating that the hot spot had been successfully removed. The remaining lines that can be seen are the Pb x-rays, a 661.6 keV ^{137}Cs line, 840.8 keV ^{54}Mn line, 1125 keV ^{65}Zn line, 1460 keV ^{40}K line, and the 2615 keV ^{208}Tl line. ^{137}Cs is a man made radionuclide with a half-life of 30.25 years. ^{54}Mn and ^{65}Zn are cosmogenics thought to be primarily in the Germanium (the Cr and Cu x-rays, respectively, are added to the gamma line energy, indicating that the decay occurs in the Germanium crystal and not in the surrounding materials) with half-lives of 312.3 and 244.3 days respectively. ^{40}K and ^{208}Tl are most likely contaminants in the detector cryostat, probably in the Copper.

2.5 One Year Underground: GATOR Background

Two of the contaminations seen in the background after the shield rebuild, ^{54}Mn and ^{65}Zn, have half lives that are less than a year. Thus after one year underground, assuming these are from cosmogenics and thus not replenished in any way, it should be possible to see a marked decrease in the strength of the associated lines. The other

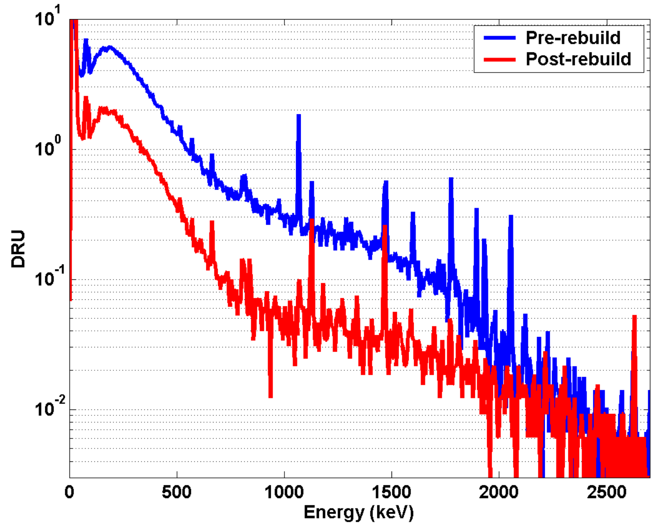

Figure 2-4. Comparison of old and new background. It is easy to see the dramatic improvement in the background after the shield rebuild. Fewer lines are apparent and the continuum spectrum is significantly lower. The old background measurement is the aforementioned 44 kg days from 7-12-2005 to 8-3-2005 while the new background run was over 57 kg days from 11-11-2005 to 12-8-2005.

sources of background are not expected to noticeably change due to much larger half-lives. Figure 2-5 shows the post shield rebuild background along with the background one year later. A decrease in both lines can in fact be seen. A full Monte Carlo simulation of the background will be presented and actual activities will be calculated in the Section 2.7.

2.6 LNGS: GATOR Background

Although all of the data obtained for this thesis was from GATOR installed in the SOLO facility, it is of passing interest how the background compares after GATOR is installed in a new shield in LNGS (Lbaoratori Nazionali del Gran Sasso or Gran Sasso National Laboratory). As opposed to sharing a shield with another detector, the LNGS shield system was built and designed solely for the GATOR detector. Fundamentally the shield structure is the same as the one in SOLO, the innermost Lead being of a lower activity than the bulk of the Lead shield. Since the Lead for this shield was purchased specifically for this application it is easier to insure that the Lead is of the lowest activity

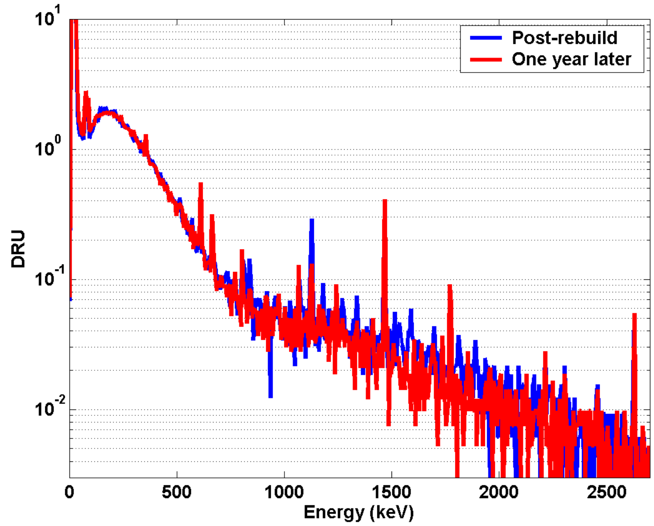

Figure 2-5. Comparison of the background post shield rebuild and one year later. The newest background run was taken from 11-14-2006 to 12-20-2006 for a total of run time of 35.7063 days.

possible. The main difference and improvement for the LNGS shield was the addition of an ultra pure, low activity Copper shield layer between the detector and the innermost Lead layer. This should have the effect of cutting down the lower energy continuum that dominated the SOLO background.

Figure 2-6 shows a comparison of the most recent SOLO background with the new background at LNGS. Although a full analysis of this new background is beyond is not presented here, it is quite clear that the new shield is far superior to the old one. Additionally, even though the GATOR detector spent several months above ground during the transport from Minnesota to Italy, the cosmogenic background does not seem to be problematic. Further screening with the GATOR detector will be much benefited from this new installation.

2.7 Simulations and Analysis: GATOR Background

All of the simulations created for the GATOR detector and various XENON detectors were created using the Geant4 simulation package created and supported by the Geant4

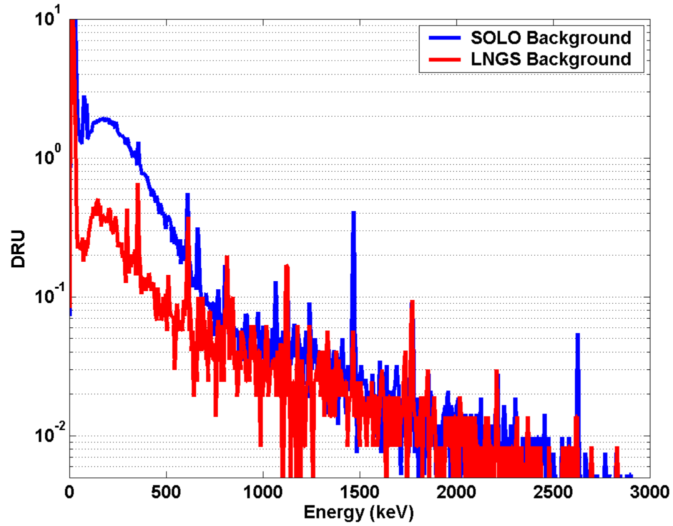

Figure 2-6. Comparison of the background at SOLO and the background at LNGS. The LNGS background was taken in the Fall of 2007 with a total run time of 14.897 days.

group primarily located at CERN[3] . The Geant4 package, in use by such collaborations as ATLAS, LISA, CMS and others, allows for very tight control over the geometry implemented, the accuracy desired and the physics processes implemented. With the different simulations needed by the XENON collaboration, the Geant4 simulation package is the perfect application. Most of the significant components that comprise the GATOR detector were simulated within a Geant4 geometry. The Germanium crystal including a dead layer from the electrodes, all of the Copper structures, several teflon pieces, and both types of Lead within the shield form the majority of the components included in the simulation. Figure 2-7 shows a side view of this detector geometry implementation. The detector is symmetric along the axis not displayed. Note that the DIODE-M detector operated by Brown is not simulated. Simulations of a high activity sample within the DIODE-M cavity indicate that only a decently high activity within the other chamber

[3] More information regarding this software package can be found at http://geant4.web.cern.ch/geant4/

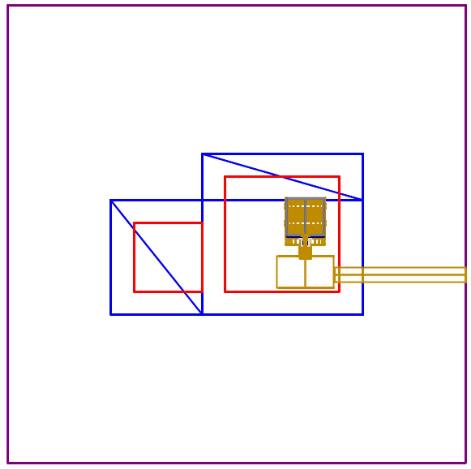

Figure 2-7. Side view of the GATOR geometry located at SOLO. The purple lines delineate the newer, higher background Lead. The blue lines indicate the older, lower background Lead. Note that the diagonal lines are merely artifacts of the 3D viewer. The red squares are the two inner cavities, one for GATOR and one for DIODE-M.

will be seen within the GATOR detector. Due to this, the regular components of the DIODE-M detector, themselves fairly low in activity, are not simulated. A standard background simulation will include decays within the Copper, the innermost layer of Lead as well as the crystal itself. It is believed the other components do not contribute significantly to the background. After the shield rebuild a brief effort was made to breakdown the majority of the GATOR backgrounds. ^{210}Bi was simulated originating from a thin layer of Lead surrounding the detector (total mass 41.36 kg). The brehmstrahlung radiation from the ^{210}Bi is responsible for a large portion of the low energy background continuum seen. ^{238}U, ^{232}Th, ^{40}K, and ^{60}Co were simulated originating from the Copper portions of the detector (total mass 5.76 kg). The second analysis procedure described in Section 3.1 was used to determine the activities of the various decays. The Lead bricks were found to have an activity of 3.013 Bq/kg of ^{210}Bi. The activity of the Copper was determined to be approximately 3.018 / 1.709 / 15.50 / 0.431 mBq/kg (U / Th / K / Co). See Figure 2-8 for the fitting plots.

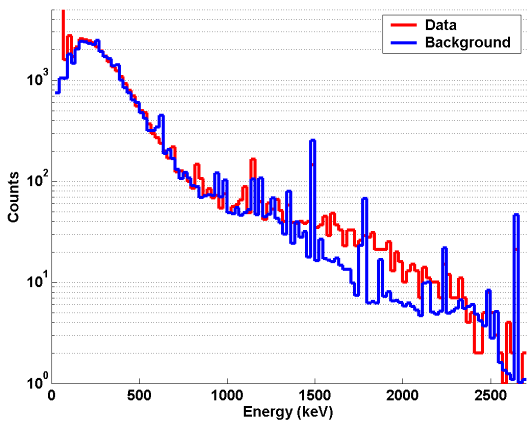

(a)

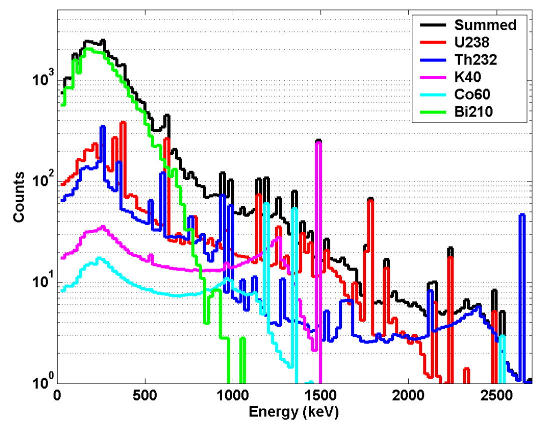

(b)

Figure 2-8. Background simulations for the GATOR Detector.
A) Background data, normalized to DRU, and the corresponding fitted simulation of radiation within the Lead and the Copper. The amount by which the individual decays have to be scaled to allow for the best fit gives an estimate on the activity of the decays in the material.
B) Shown here are the five individual decays that make up most of the GATOR background. The Bismuth was simulated within a small layer of Lead on the inside of the cavity while the Uranium, Thorium, Potassium and Cobalt are simulated within all of the Copper used in the detector's construction.

The same procedure was done on the background data taken one year after the shield rebuild as well. The numbers were not significantly changed, nor were they expected to. ^{210}Bi in the Lead was calculated to 3.103 Bq/kg, very similar to before. The activity of the Copper was determined to be approximately 2.813 / 1.434 / 15.45 / 0.285 mBq/kg (U / Th / K / Co), again not to much different from the previous analysis.

A more complete analysis was done to additionally determine the activity of the ^{137}Cs, ^{54}Mn, and ^{65}Zn contaminations. ^{238}U and ^{232}Th were additionally simulated within the Lead layer, ^{137}Cs, ^{54}Mn and ^{65}Zn were simulated within the Copper and ^{65}Zn and ^{54}Mn were simulated within the outermost crystal surface (0.134026 kg mass). Again, the values as determined before are little changed. Table 2-2 shows the calculated activities. For most of the the runs listed here, 10 simulations of 1e6 events were added together for a total of 1e7 events for each decay. The ^{210}Bi simulation required 1e8 total events

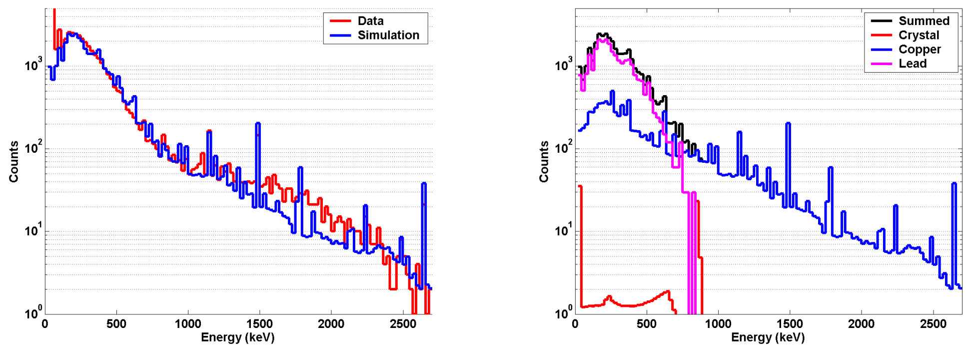

(a) (b)

Figure 2-9. More advanced GATOR Background simulations.
A) Data from the GATOR Background (in red) compared to the Monte Carlo simulation (in black).
B) Histograms of the summed Copper, Lead and crystal activities used to create the total Monte Carlo approximation. The crystal values at around 10^{-2} have no visible effect on the total simulation.

for decent statistics. The ^{238}U and ^{232}Th values from the Lead are so small as to be totally negligible. The ^{54}Mn and ^{65}Zn values are somewhat entangled and it is difficult to determine how much is from the Copper and how much is from the crystal, making these values somewhat suspect.

Table 2-2. Background activity data using the fitting method.

Line	Scale Factor	Activity (mBq/kg)
^{238}U	2.20e-6	2.20
^{232}Th	1.32e-6	1.32
^{40}K	8.76e-6	8.76
^{60}Co	1.88e-7	0.188
^{137}Cs	2.75e-7	0.276
^{65}Zn	7.46e-8	0.0746
^{54}Mn	7.38e-11	7.38e-5
^{210}Bi (Pb)	1.67e-2	23.3 Bq/kg
^{238}U (Pb)	7.48e-12	1.04e-6
^{232}Th (Pb)	5.64e-12	7.86e-7
^{65}Zn (Ge)	5.17e-10	6.77e-4
^{54}Mn (Ge)	1.36e-8	.0179

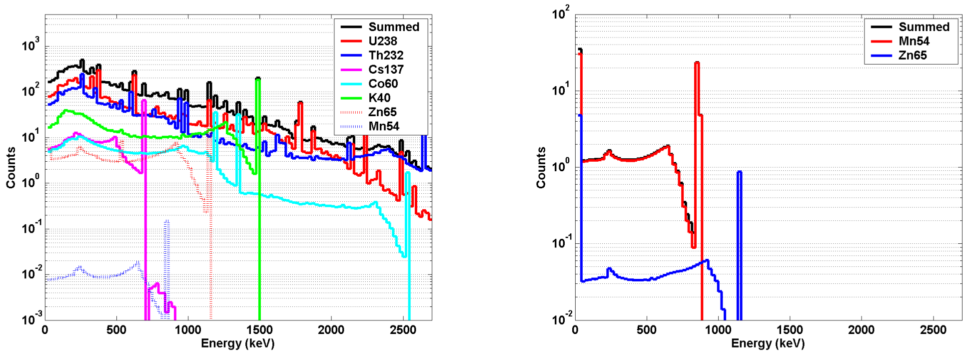

(a) (b)

Figure 2-10. Copper and crystal portions of the GATOR Background simulation. A) The individual decays that comprise the Copper simulation. Due to the tiny contribution from Mn54, to fully display all of the decays the y axis has a different scaling than the plots above.
B) The individual decays that comprise the crystal simulation. Given how small the contribution from the crystal simulation is, note the different scaling on the y axis.

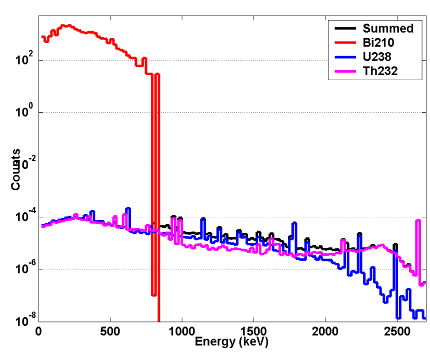

Figure 2-11. Lead portion of the GATOR Background simulation, showing individual decays that comprise the Lead layer simulation. Due to the wide range of activities calculated within the Lead simulation, again note the y scaling is different than the other plots.

2.8 Radon Contamination

One of the highest background sources that we have to deal with is Radon gas in the air. It is important to understand the influence of a Radon contamination on the data. Even though keeping the detector chamber filled with a positive pressure of nitrogen gas can eliminate most of this Radon, it is possible for the Radon purge to slow down or turn off completely during a given run.

A large Radon contamination was introduced into the GATOR chamber between 5/2/2006 8:31 AM and 5/4/2006 8:35 AM whilst sampling the 6 poly bricks that will be discussed in greater detail later. It is also possible that a small Radon contamination may have been present from the beginning of the run, but the data is not conclusive until 233 hours into the run.

The first and simplest way to discover a Radon contamination is to look for the presence of any strong Radon lines in the spectrum. The blue line displayed in Figure 2-12 is the data after 185 hours of live time while the red line is the data after 233 hours, a mere 48 hours later. Notice that there are now several very strong lines visible, all of which can be attributed to Radon decay. To more carefully analyze this Radon contamination we'll focus on three different time periods. The first is from the beginning of the run, 4/14/2006 - 4/19/2006. Figure 2-13 shows the one Radon line (351.9 keV) and the 1460 keV Potassium line with time on the x axis and counts per hour on the y axis. A decrease in the counts per hour for the Radon line can be observed, possibly indicating that a small amount of Radon was present in the cavity at the start of the run but was subsequently purged by the nitrogen. The second region of time occurs immediately following the first one, from 4/19/2006 - 4/24/2006. Figure 2-14 shows the same type of information as Figure 2-13, but there again is nothing definitive. The Radon line shows a slight increase in the counts per hour, however since the change is so small, roughly 0.1 counts per hour, it is not possible to say whether this increase comes from a small increase in the Radon level or a random statistical fluctuation. The most interesting period of

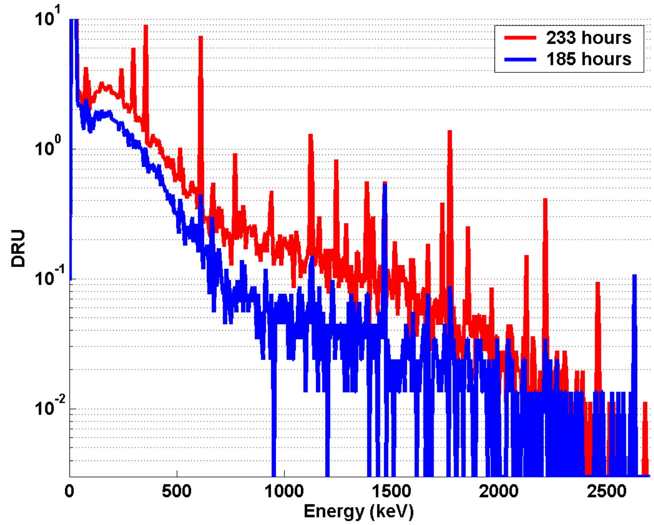

Figure 2-12. Data from the poly shield bricks after 185 hours (blue line) and after 233 hours (red line). The many strong peaks visible originate from Radon decay in the air surrounding the detector. And their presence appearing within a 48 hour time period during the middle of the run strongly indicates a Radon leak during that time.

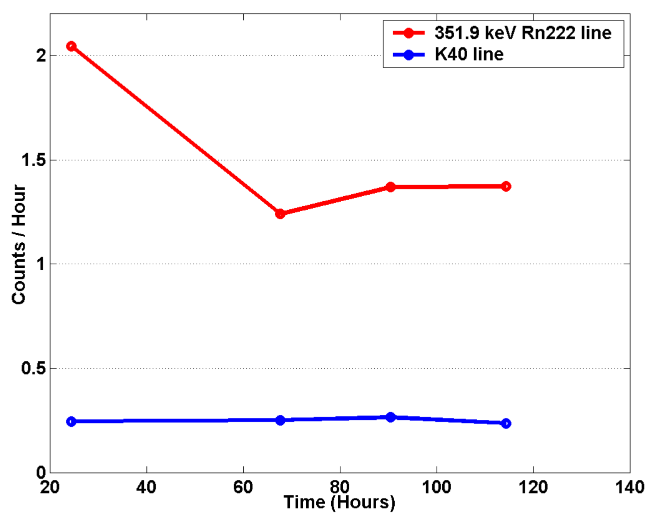

Figure 2-13. The Radon purge in action, showing counts per hour versus time, displaying one line originating from Radon (red) and the one line originating from Potassium (blue). Note how the Radon line shows a decline in the early hours while the Potassium line holds steady. This data comes from the first 5 days of data taking.

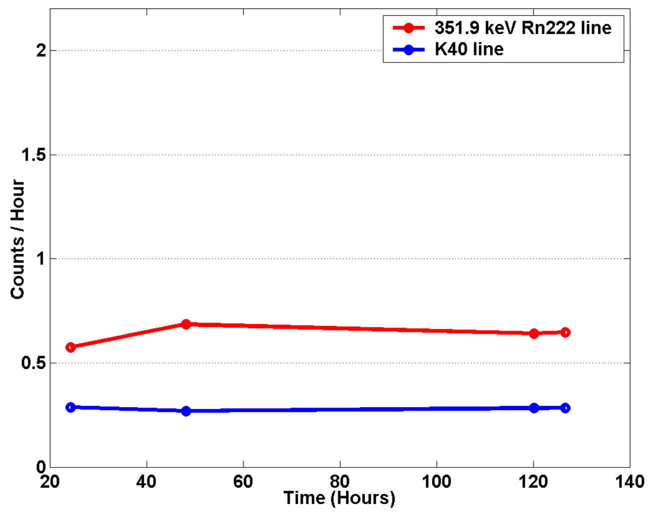

Figure 2-14. Counts per hour versus time during the middle of the run, showing one line originating from Radon (red) and the one line originating from Potassium (blue). The slight increase in frequency for the Radon line could be indicative of Radon present in the cavity but due to how small it is nothing can be said with any certainty. This data comes from the 6th through 10th days of operation.

time is from 4/24/2006 - 5/19/2006. It is in this region that a large influx of Radon shown in Figure 2-12 can be seen. Figure 2-15 displays six of the Radon lines and the Potassium line, showing counts as a function of time. It is readily apparent that between 185 hours and 233 hours the strength of the Radon lines dramatically increases while the Potassium line does not. Looking at the counts per hour as a function of time, shown in Figure 2-15, confirms this. It is very apparent that the counts per hour for the Radon line greatly increases while the counts per hour for the ^{40}K line remains relatively constant.

2.9 Data Acquisition Failure

The apparent fall off in Figure 2-15 cannot be solely explained by the Radon being purged from the chamber. Between 258h and 401.2h the data acquisition seems to have halted. Although the live time recorded by the software continues to increase, the number of counts in the entire spectrum remains constant. This can also be seen in Figure 2-15 as a plateau in the data. This false drop off comes from the fact that the time is increasing

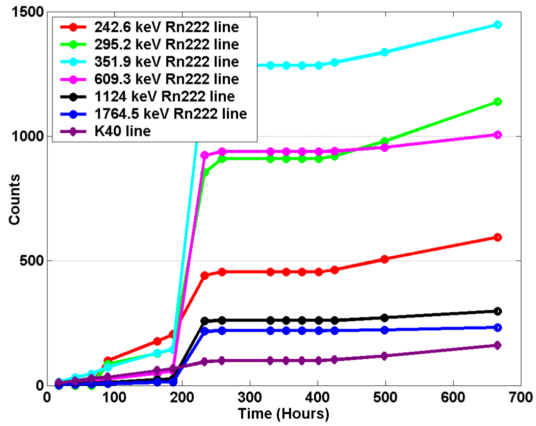

(a)

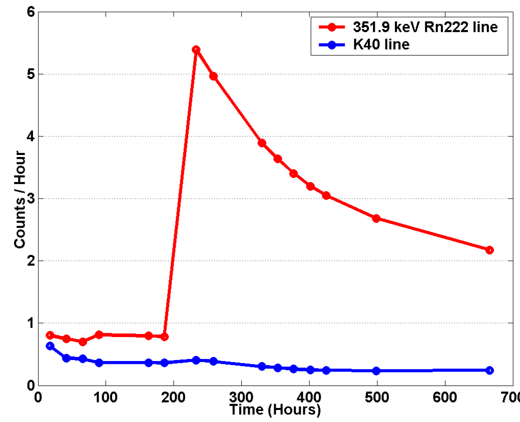

(b)

Figure 2-15. When Radon was introduced, showing counts and counts per hour.
A) Number of counts versus time, showing six lines originating from Radon and one line originating from Potassium (purple). The dramatic increase in the number of counts from Radon while the Potassium remains unaffected is clear indication of a Radon contamination.
B) Number of counts per hour versus time, showing one line originating from Radon (red) and the one line originating from Potassium (blue). The decrease in counts per hour arises not from a lessening in the Radon level but instead from a hardware issue that resulted in a loss of data.

while the data does not, thereby lowering the number of counts per hour. This loss of data acquisition occurred some time between 5/5/2006 9:30 AM and 5/11/2006 9:00 AM. The above analysis detailing the data acquisition failure and the Radon contamination serve to demonstrate the other types of information that can be obtained from GATOR data. While it is true that the main information of interest is the activities of the screened materials (Chapter 3) it can occasionally be important to use the data to determine something in regards to the operation of the detector itself.

CHAPTER 3
GATOR MATERIAL SCREENING

3.1 Analysis Procedures

There are two methods that are used to calculate the activity of a decay chain. The first method which will be used to determine the activities of the samples looks at the number of counts in a representative photopeak and compares that to the background. Combining the counts due solely to the radioactive decay with the peak detection efficiency will translate directly into an activity.

The activity of a given line is calculated using Equation 3–1.

$$Activity(Becquerrel \cdot kg^{-1}) = \frac{D - B}{E \cdot m_{sample}} \tag{3–1}$$

where D is the number of counts per second due to the data, B is the number of counts per second due to the background, E is the efficiency determined from Monte Carlo simulations and m_{sample} is the mass of the sample (or the number of PMTs for example). The efficiency of a given line is calculated via a Monte Carlo simulation, by randomly starting the chosen decay within the sample volume and observing the photons that react with the sensitive detector volume.

$$Efficiency = \frac{Counts - in - photopeak}{Events - simulated} \tag{3–2}$$

To determine the number of counts from a given line, a 3-sigma region, roughly 9 bins or approximately 6 keV, centered on the line was used. This range was determined by fitting a gaussian to the ^{60}Co peaks and the ^{40}K peaks and calculating the sigma. To determine the 3-sigma region at lower energies, lines originating from radon decay (351.9 keV and 609.3 keV) were also fitted with a gaussian, confirming that a 9 bin spread will be an adequate range at these energies.

As mentioned before, calculating the efficiency of a given line requires Monte Carlo simulation (method 2 described below also requires the use of simulations). Using Geant4, the various samples are modeled and the complete decay chains simulated from within the appropriate volumes.

The value reported for a given activity is usually an average of two activities obtained from two different lines. For the Uranium decay the ^{214}Pb and ^{214}Bi decays are used, for the Thorium decay the ^{224}Ac and low energy ^{212}Po decays are used. These four decays provide the strongest and by far the most prominent gamma lines for these two decays making them the easiest and sometimes the only detectable lines present. Only the one ^{40}K line is used for the Potassium decay while both main lines from ^{60}Co are used for the Cobalt decay. The single ^{137}Cs is used for the Cesium decay.

Calculating the error for the activities calculated using the above method is fairly straight forward. We define the error in the number of counts in a given peak using Equation 3–3.

$$Error(Bq/kg) = \frac{\sqrt{D_1}}{m_{sample} \cdot E} \tag{3–3}$$

where D_1 is the number of counts per second in a given peak from the data run, m_{sample} is again the mass or number of the sample, and E is the efficiency calculated as described above. Note that calculating the error in this fashion only works when there's enough statistics above the background. When not enough statistics are present to determine an actual value for the activity (indicated by a negative value for the activity) the value calculated via the following method is used.

The second method used is to take the Monte Carlo simulations for each decay chain and scale the spectra such that they fit the data. When the data is scaled such that the y-axis is in differential count rate (DRU: events $\cdot kg^{-1} \cdot day^{-1} \cdot keV^{-1}$) the activity can be calculated via Equation 3–4.

$$Activity(events \cdot kg^{-1} \cdot day^{-1}) = \frac{N \cdot m_{det} \cdot binwidth \cdot scale}{m_{sample}} \tag{3–4}$$

where, N is the number of events simulated, $m_{detector}$ and m_{sample} are the mass of the detector and sample respectively, *binwidth* is the size of the bins in keV, and *scale* is the factor by which the simulation needs to be scaled in order to best fit the data. This scaling factor is calculated by attempting to minimize the chi-squared value for different fits, determined bin by bin. This fit is done over the relevant energy range, roughly 200 keV to 1500 keV (the lowest and highest energies show an ignorable discrepancy between simulation and data). To facilitate the fitting of multiple decays, a simple program was written that varies one of the spectra while keeping the others constant.[1]

For all samples, both of these methods will be used to calculate the activities. Please refer to the individual sections for specifics.

3.2 Overview of Screened Materials

Table 3-1 is provided to allow for easy reference for all screened items. Each of the following sections will include the appropriate values from Table 3-1, as well as the data and plots used to calculate these values.

Table 3-1. Summary of results for all samples screened thus far at SOLO in Soudan.

Sample	Activity (U / Th / K / Co / Cs)
SS from UF OC	mBq/kg (NA / NA / 7.13±3.11 / 67.57±1.59 / NA)
R8520 PMTs	mBq/PMT (15.79±5.34 / 11.3 / 110.3±41.4 / 2.13 / 1.46)
Cirlex PMT Bases	mBq/Base (1.21±0.293 / 1.07 / 6.68±1.24 / 0.0712 / 0.126)
SS from Xe-10 spare IC	mBq/kg (13.43±5.22 / 44.07±6.66 / 116.94±24.3 / 7.30 / 5.98)
Poly shield bricks	mBq/kg (22.3±3.10 / 2.53±2.08 / 53.2±14.53 / 1.06 / 0.663)
Teflon from Xe-10 ID	mBq/kg (15.0 / 5.54 / 60.69±24.12 / 1.67 / 1.21)
Sample Z, 2 large FT's	mBq/FT (55.6 / 0.28 / 157 / 9.12±1.48 / 9.33)
Sample H, SS for elecrodes	mBq/kg (772 / 342 / 1070 / 12.1 / 2.90±6.24)

3.3 Stainless Steel-304, Sample Taken From the UF XENON Outer Cryostat

The first stainless steel sample measured was a remnant from the UF's XENON Prototype Outer Cryostat, originally purchased from the A+N Corporation. The activity in this sample was completely dominated by the two high energy ^{60}Co lines. In Figure 3-2, it can be seen that all lines of lower energy than the ^{60}Co lines are buried in

[1] This fitting code can be found at www.phys.ufl.edu/xenon/Fitting_Code.doc

the continuum originating from the compton scattering of these lines. The activity of the sample was calculated to be

mBq/kg (NA / NA / 7.13±3.11 / 67.57±1.59 / NA) (U /Th / K / Co / Cs)

Table 3-2 shows the numbers used to calculate the activity via the first analysis procedure discussed. The live time for this sample was 12.5945 days and the sample mass was 3.407 kg. Table 3-3 shows the numbers used to calculate the activities using the fitting method discussed above. Given how the ^{238}U and ^{232}Th lines are subsumed by the ^{60}Co spectrum, the calculated activities are likely inaccurate. However cobalt is typically the dominant source of radiation from steel so these decays can safely be ignored in this case anyways. The comparison of fit to data and the individual decays can be seen in Figure 3-3.

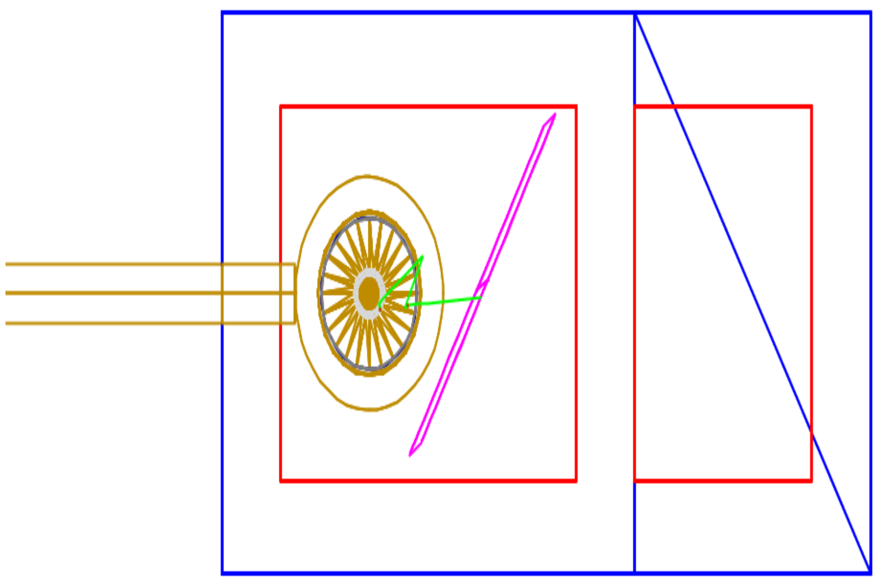

Figure 3-1. Image created using the Geant4 simulation, showing a top down view of the detector cavity and the steel sample. The green track is one simulated Cs137 decay originating from within the sample volume.

Table 3-2. First stainless steel sample activities using the background comparison method.

Line Energy (keV)	Bkg (cnts)	Data(cnts)	Efficiency	Activity (mBq/kg)
^{40}K (1460.8)	115	76	7.56e-4	7.13±3.11
^{60}Co (1173.2)	30	1900	7.49e-3	67.9±8.7
^{60}Co (1332.5)	25	1747	6.95e-4	67.3 ±8.5

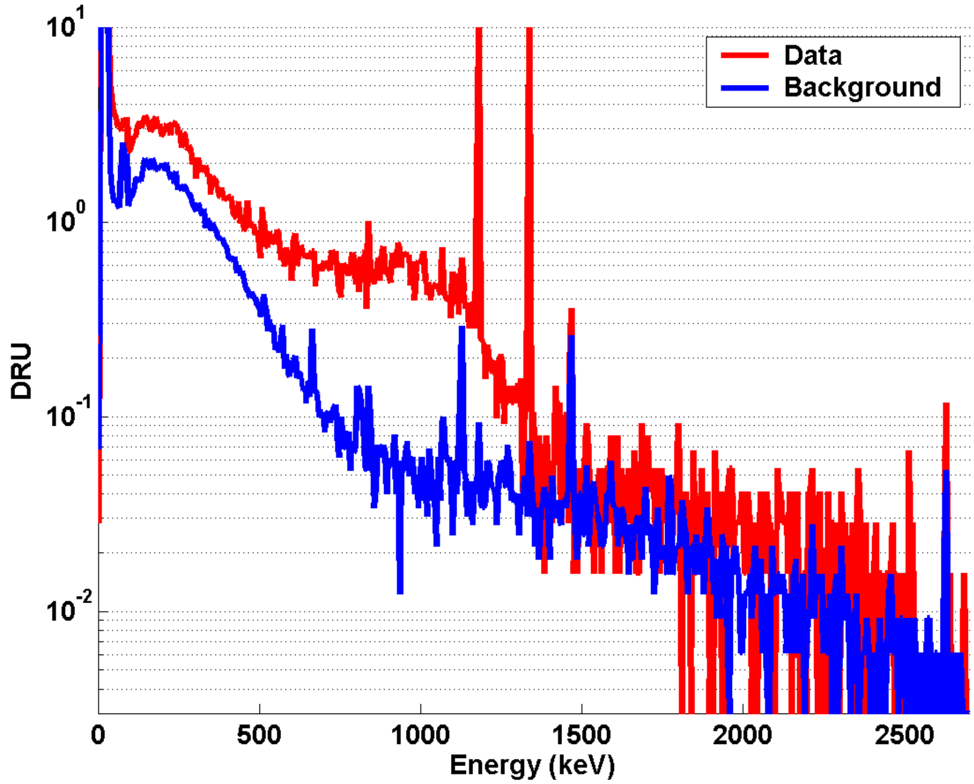

Figure 3-2. Background data and steel sample data, normalized to DRU. The background used is the new background taken over 25.8511 days. The spectrum for the steel sample was taken over 12.4945 days from 1-3-2006 to 1-13-2006.

Table 3-3. First stainless steel sample activities using the fitting method.

Line	Scale Factor	Events Simulated	Activity (mBq/kg)
^{238}U	1.59e-11	1.00e12	2.70
^{232}Th	1.59e-11	5.00e10	0.14
^{40}K	2.72e-8	5.00e8	2.30
^{60}Co	3.88e-5	1.00e7	65.7

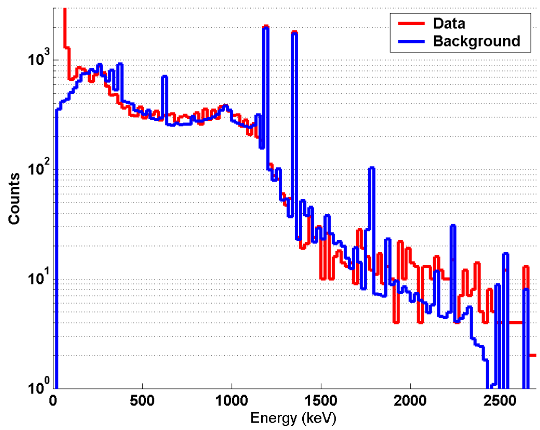

(a)

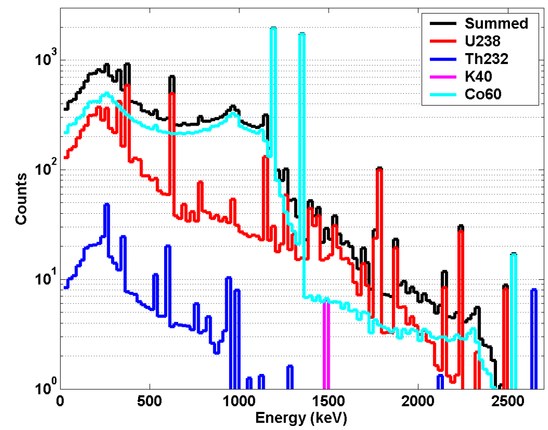

(b)

Figure 3-3. Steel data with background subtracted compared to simulation.
A) Background subtracted steel data from UF's XENON Prototype Outer Cryostat remnant compared to the Monte Carlo simulation. In this simulation, the two ^{60}Co gamma rays were assumed to be emitted with 100 percent efficiency, with the origin of the decay and the direction of the two gammas randomly placed within the steel sample geometry.
B) Histograms of the various decays used to create the summed spectrum used in the left plot.

3.4 Hamamatsu PMTs, R8520

Four of the one inch square PMTs from Hamamatsu were placed in a semi-circular arrangement around the detector. Hamamatsu has also provided all of the materials used to make the PMTs which will be screened in the future, possibly allowing Hamamatsu to understand the material that provides the dominant background and facilitating the design of newer, lower background PMTs. Because of the location of the PMTs within the inner detector, they appear to be the dominant source of background in the XENON10 detector. The activity of the sample was calculated to be

mBq/PMT (15.79±5.34 / 11.3 / 110.3±41.4 / 2.13 / 1.46) (U /Th / K / Co / Cs)

Table 3-4 shows the numbers used to calculate the activity via the first analysis procedure discussed. Table 3-5 shows the numbers used to calculate the activities using the fitting method discussed above. Figure 3-6 shows the fit to data and the individual decays.

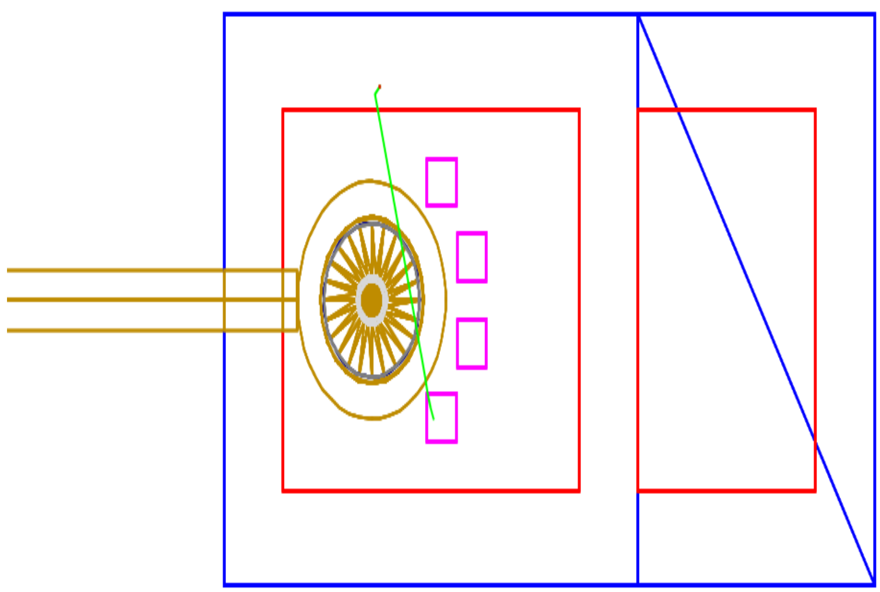

Figure 3-4. Photomultiplier tube sample placement within the Monte Carlo simulation.

Table 3-4. Four PMT activities using the background comparison method.

Line Energy (keV)	Bkg (cnts)	Data(cnts)	Efficiency	Activity (mBq/kg)
U (^{214}Pb)(351.9)	388	439	3.15e-4	18.43±7.46
U (^{214}Bi)(609.3)	82	128	3.94e-4	13.14±3.22
^{40}K (1460.8)	115	147	3.29e-5	110.3±41.4
^{137}Cs (661.6)	118	112	6.94e-4	1.01±1.76

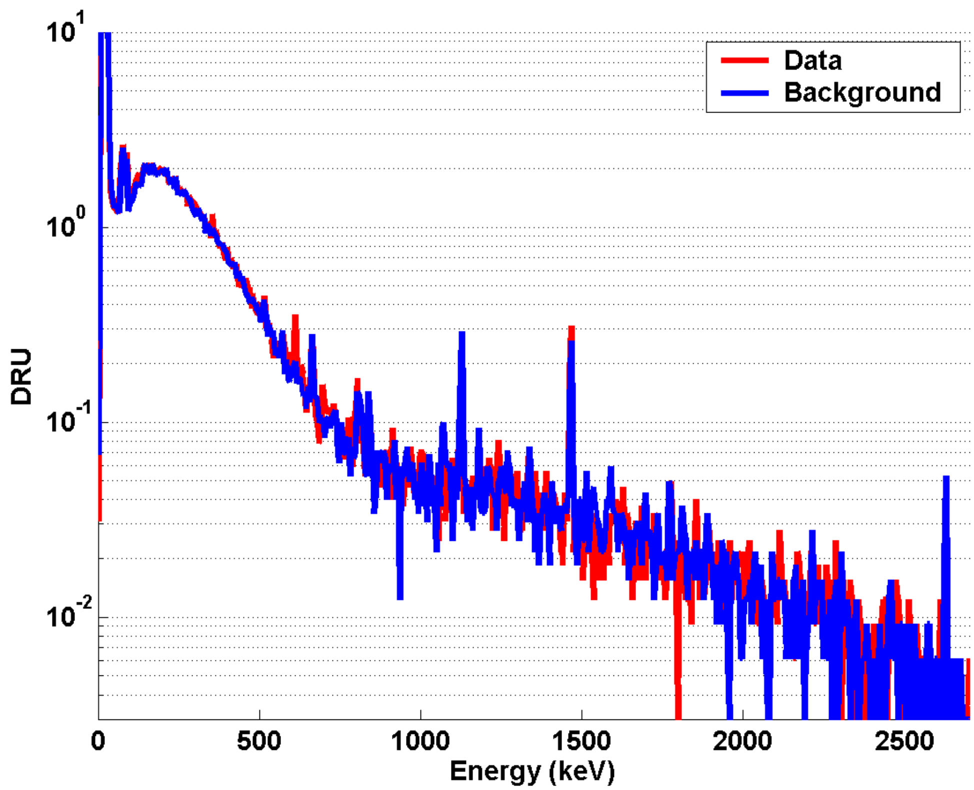

Figure 3-5. Photomultiplier tube sample data and background data, normalized to DRU. The background used is the new background taken over 25.8511 days. The spectrum for the pmt sample was taken over 25.798 days from 12-8-2005 to 1-2-2006.

Table 3-5. Four PMT activities using the fitting method.

Line	Scale Factor	Events Simulated	Activity (mBq/kg)
^{238}U	1.50e-4	1e6	21.7
^{232}Th	7.85e-5	1e6	11.3
^{40}K	5.84e-5	1e7	84.1
^{60}Co	1.48e-6	1e7	2.1
^{137}Cs	1.01e-6	1e7	1.5

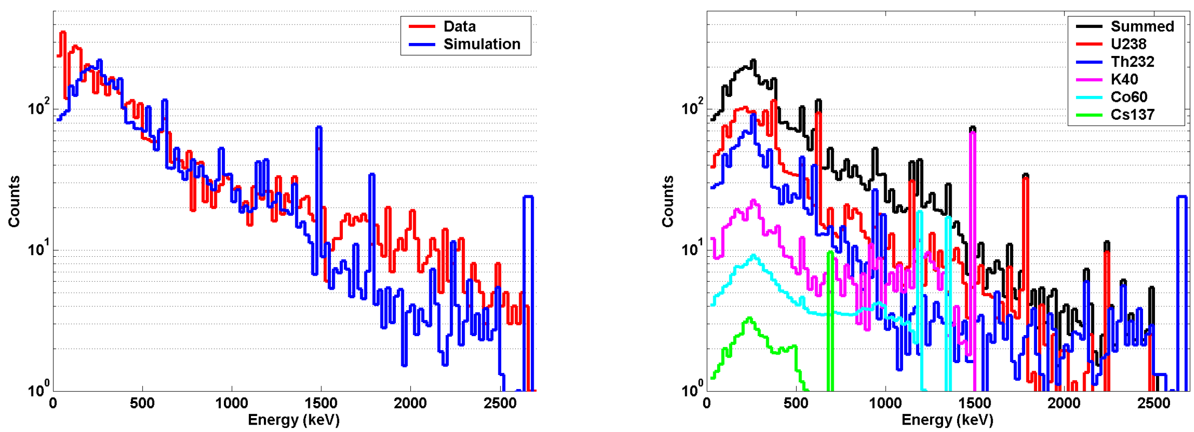

(a) (b)

Figure 3-6. Photomultiplier tube data with background subtracted compared to simulation.
A) Background subtracted data from the four R8520 Hamamatsu PMTs compared to the Monte Carlo simulation.
B) Histograms of the various decays used to create the summed spectrum used in the left plot.

3.5 Cirlex PMT Bases

Each PMT is attached to an approximately one inch square circuit board at the base. 45 of these Cirlex bases ($C_{22}H_{10}N_2O_5$), weighing approximately 83 grams were placed within the detector sealed within a plastic bag. At some point in the past, our collaborators at Brown measured a large pile of such plastic bags and were unable to detect any intrinsic radiation within them, thus the data in this case should solely be from the Cirlex. The activity of the sample was calculated to be

mBq/Base (1.21±0.293 / 1.07 / 6.68±1.24 / 0.0712 / 0.126) (U /Th / K / Co / Cs)

Table 3-6 shows the numbers used to calculate the activity via the first analysis procedure discussed. Table 3-7 shows the numbers used to calculate the activities using the fitting method discussed above. Figure 3-9 shows the fit to data along with the individual decays for the Cirlex simulation.

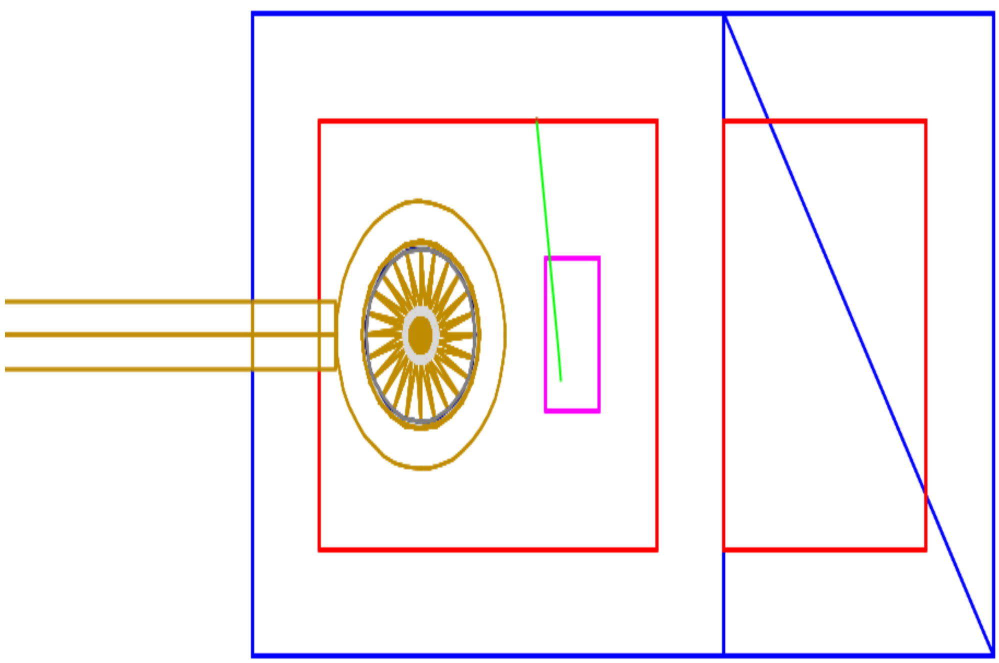

Figure 3-7. Cirlex PMT base sample placement within the Monte Carlo simulation.

Table 3-6. Cirlex PMT base activities using the background comparison method.

Line Energy (keV)	Bkg (cnts)	Data(cnts)	Efficiency	Activity (mBq/kg)
U (^{214}Pb)(351.9)	388	358	6.41e-4	2.06±0.442
U (^{214}Bi)(609.3)	82	82	7.94e-4	0.471±0.171
^{40}K (1460.8)	115	145	1.39e-4	6.99±1.29
^{137}Cs (661.6)	105	112	1.38e-3	0.282±0.106

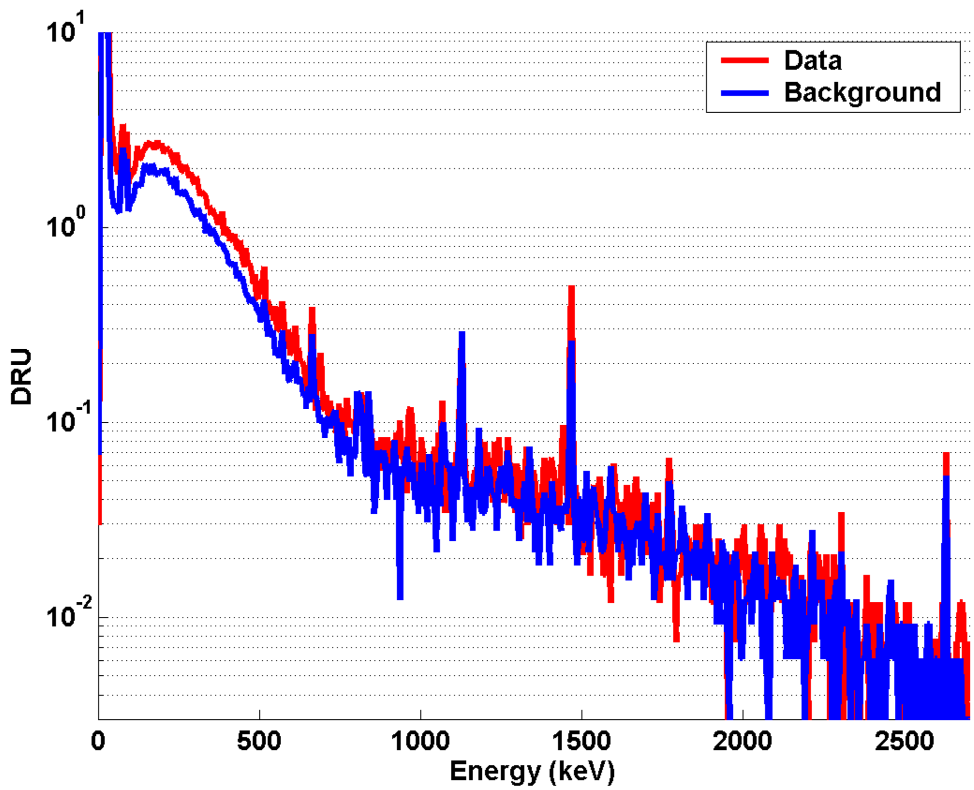

Figure 3-8. Cirlex sample data and background data, normalized to DRU. The background used is the new background taken over 25.8511 days. The spectrum for the Ccirlex sample was taken over 17.979 days from 1-17-2006 to 2-14-2006.

Table 3-7. Cirlex PMT base activities using the fitting method.

Line	Scale Factor	Events Simulated	Activity (mBq/kg)
^{238}U	1.46e-4	1e6	1.9
^{232}Th	8.35e-5	1e6	1.1
^{40}K	6.11e-5	1e7	7.8
^{60}Co	5.56e-7	1e7	0.071
^{137}Cs	9.86e-7	1e7	0.13

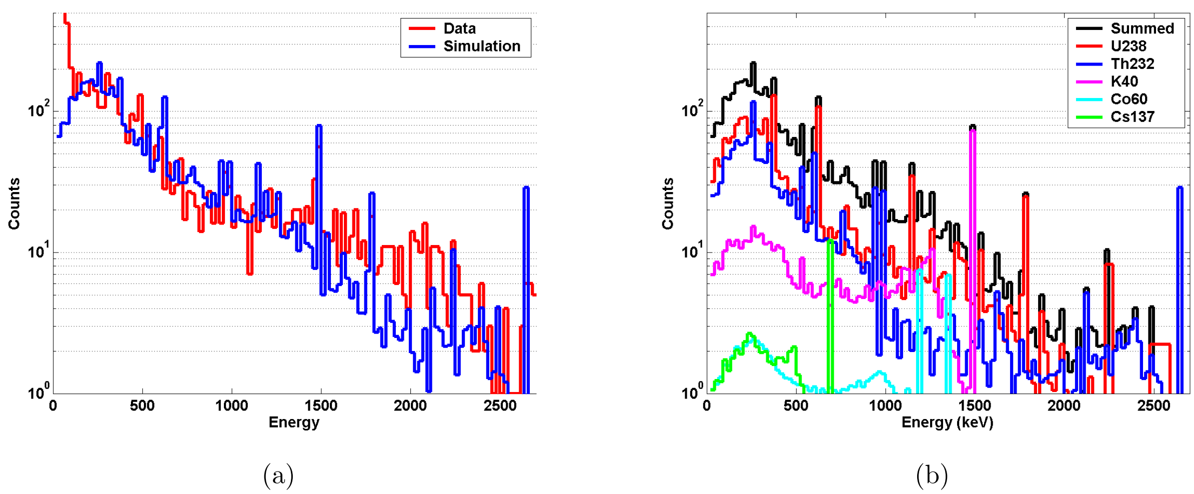

Figure 3-9. Cirlex data with background subtracted compared to simulation.
A) Background subtracted data from the 45 Cirlex PMT bases (83g in total) compared to the Monte Carlo simulation.
B) Histograms of the various decays used to create the summed spectrum used in the left plot.

3.6 Stainless Steel-304 Sample From XENON10 Spare Inner Cryostat

Due to the extremely high background from a piece of steel not being used within the detector, a piece of steel from the spare XENON10 Inner Cryostat was also measured. The Co^{60} was not totally dominant in this sample making it possible to estimate all of the decays. The activity from this sample is the one that is used in the XENON simulations as opposed to the previous steel numbers. The activity of the sample was calculated to be

mBq/kg (13.43±5.22 / 44.07±6.66 / 116.94±24.3 / 7.30/ 5.98) (U /Th / K / Co / Cs)

Table 3-8 shows the numbers used to calculate the activity via the first analysis procedure discussed. The mass of this sample was 0.4819 kg. Table 3-9 shows the numbers used to calculate the activities using the fitting method discussed above. Figure 3-12 shows the fit and the individual components.

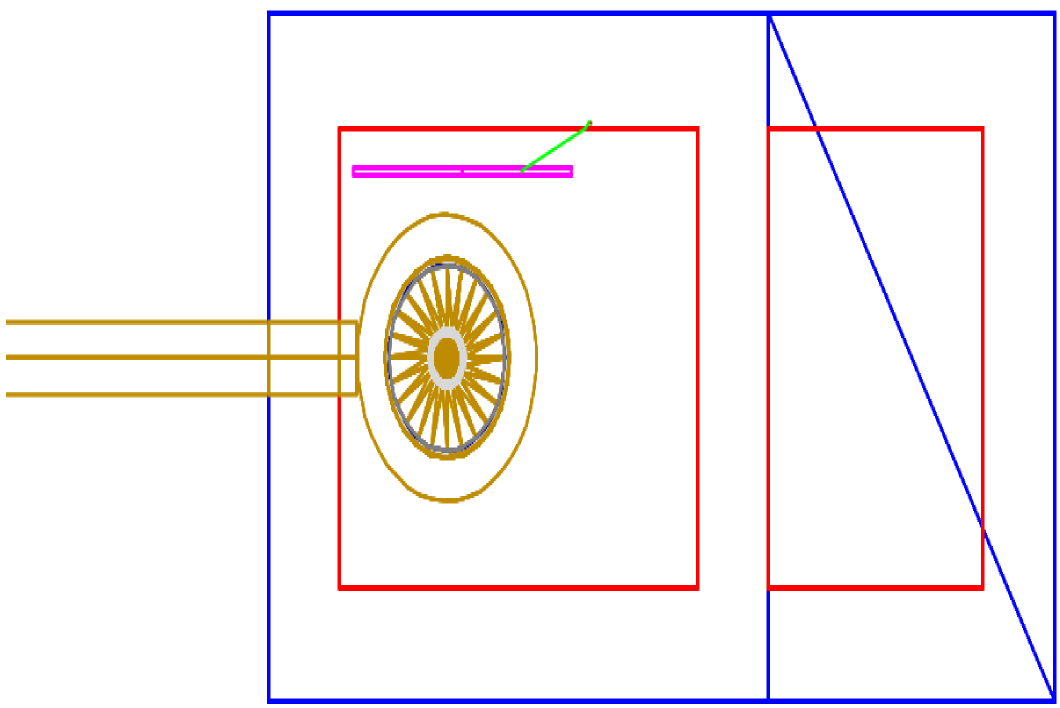

Figure 3-10. Second stainless steel sample placement within the Monte Carlo simulation.

Table 3-8. Second stainless steel sample activities using the background comparison method.

Line Energy (keV)	Bkg (cnts)	Data(cnts)	Efficiency	Activity (mBq/kg)
U (^{214}Pb)(351.9)	388	345	3.21e-3	10.48±6.62
U (^{214}Bi)(609.3)	82	112	3.16e-3	16.38±3.83
Th (^{212}Po)(583.2)	79	155	2.15e-3	48.2±6.62
Th (^{228}Ac)(911.2)	28	74	1.47e-3	39.9±6.70
^{40}K (1460.8)	115	153	5.81e-4	116.9±24.3
^{137}Cs (661.6)	126	112	6.04e-3	6.60±2.12

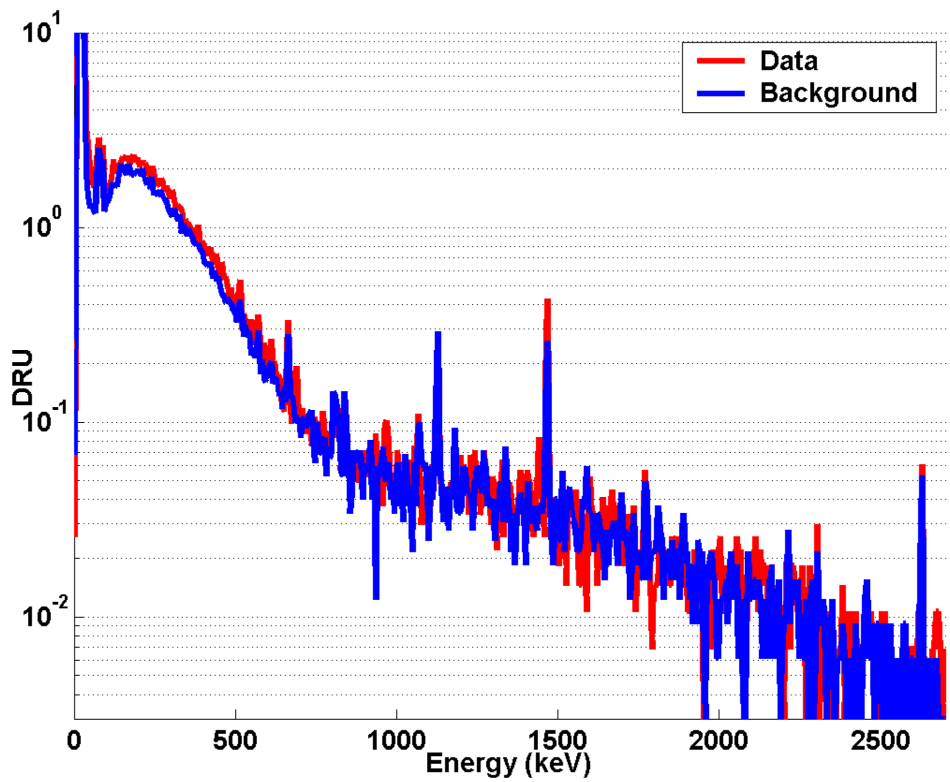

Figure 3-11. Second stainless steel sample data and background data, normalized to DRU. The background used is the new background taken over 25.8511 days. The spectrum for the steel sample was taken over 21.063 days from 2-14-2006 to 3-8-2006.

Table 3-9. Stainless steel sample activities using the fitting method.

Line	Scale Factor	Events Simulated	Activity (mBq/kg)
^{238}U	2.72e-5	1e6	32.5
^{232}Th	3.52e-5	1e6	42.1
^{40}K	4.06e-5	1e7	485
^{60}Co	6.10e-7	1e7	7.3
^{137}Cs	5.00e-7	1e7	6.0

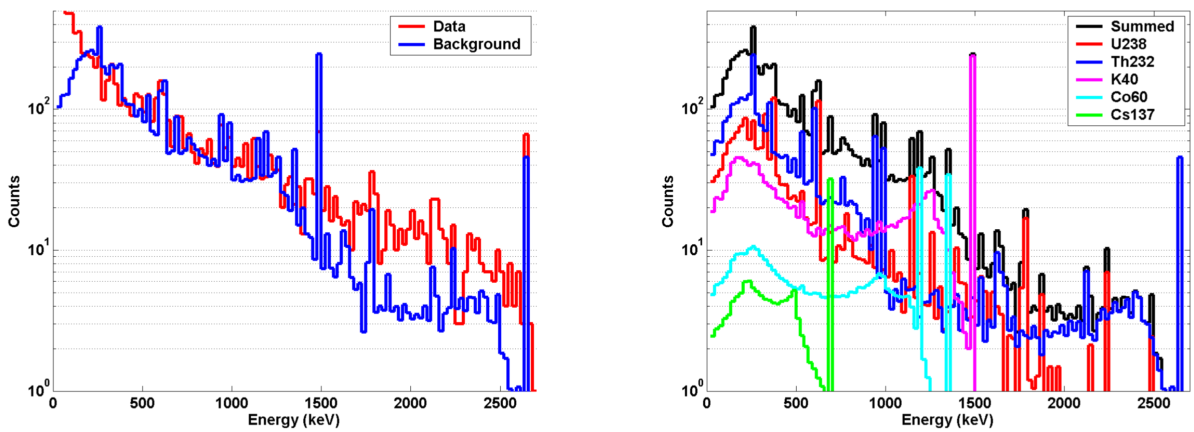

(a) (b)

Figure 3-12. Second steel sample data with background subtracted compared to simulation.
A) Background subtracted data from the stainless steel sample compared to the Monte Carlo simulation.
B) Histograms of the various decays used to create the summed spectrum used in the left plot.

3.7 Poly Bricks from KMAC Plastics, Used in the XENON10 Inner Shield

The innermost shield surrounding the XENON10 Detector is composed of polyethylene (C_2H_4) bricks that act to shield from incoming neutrons. Nothing was known of this shields activity, so six of these bricks were screened. Originally two were screened but the statistics were low enough that the time was taken to add four more bricks. At one point a radon leak occurred during the screening of these bricks, further necessitating more screening time. The activity of the sample was calculated to be

mBq/kg (22.3±3.10 / 2.53±2.08 / 53.2±14.53 / 1.06 / 0.663) (U /Th / K / Co / Cs)

Table 3-10 shows the numbers used to calculate the activity via the first analysis procedure discussed. The mass of this sample was 1.375 kg. Table 3-11 shows the numbers used to calculate the activities using the fitting method discussed above. Figure 3-15 shows the fit and the individual components. It appears that the code overestimates the amount of ^{40}K present. This effect is shown in the numbers in Table 3-11 and in the fitted simulations in Figure 3-15. Attempts to redesign the code to fit only the peaks have thus far yielded results not as accurate than currently seen.

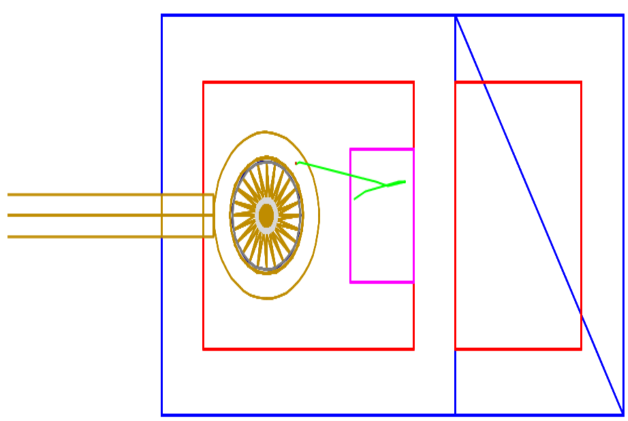

Figure 3-13. Poly brick sample placement within the Monte Carlo simulation.

Table 3-10. Poly sample activities using the background comparison method.

Line Energy (keV)	Bkg (cnts)	Data(cnts)	Efficiency	Activity (mBq/kg)
U (^{214}Pb)(351.9)	388	496	2.10e-3	27.45±4.77
U (^{214}Bi)(609.3)	82	170	2.12e-3	17.15±2.66
Th (^{212}Po)(583.2)	79	77	1.16e-3	2.47±2.67
Th (^{228}Ac)(911.2)	28	32	1.07e-3	2.59±2.65
^{40}K (1460.8)	115	145	3.08e-4	53.21±13.56

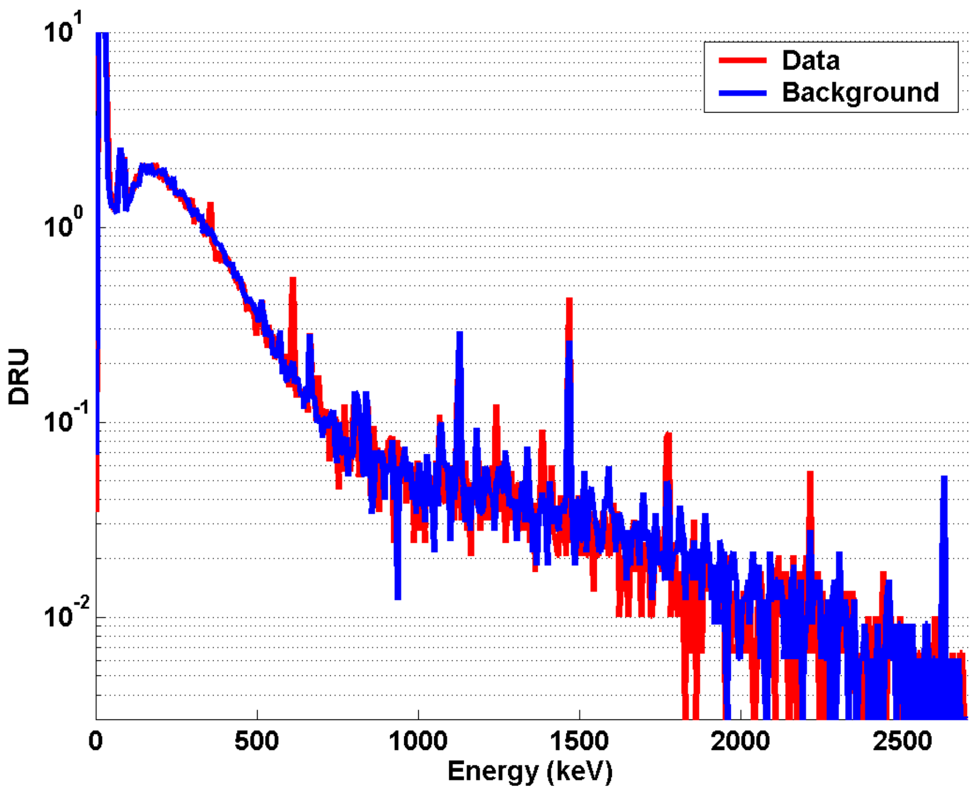

Figure 3-14. Poly sample data and background data, normalized to DRU. The background used is the new background taken over 25.8511 days. The spectrum for the poly sample was taken over 22.6786 days from 7-17-2006 to 7-25-2006 and 9-21-2006 to 10-5-2006. This is actually a recount of data taken in March through May of 2006, however a radon contamination made the data unusable.

Table 3-11. Poly sample activities using the fitting method.

Line	Scale Factor	Events Simulated	Activity (mBq/kg)
^{238}U	6.14e-6	1e7	25.8
^{232}Th	4.96e-7	1e7	2.1
^{40}K	2.54e-5	1e7	107
^{60}Co	2.54e-7	1e7	1.06
^{137}Cs	1.58e-7	1e7	0.66

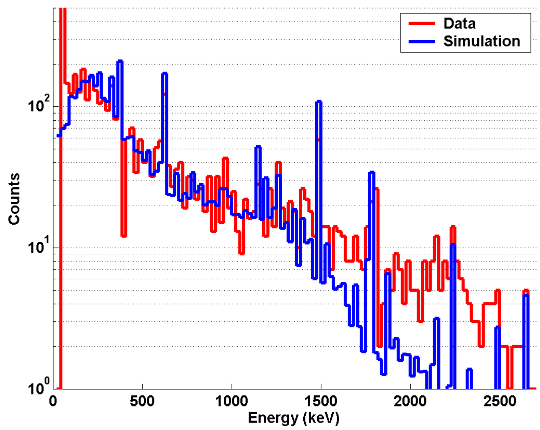

(a)

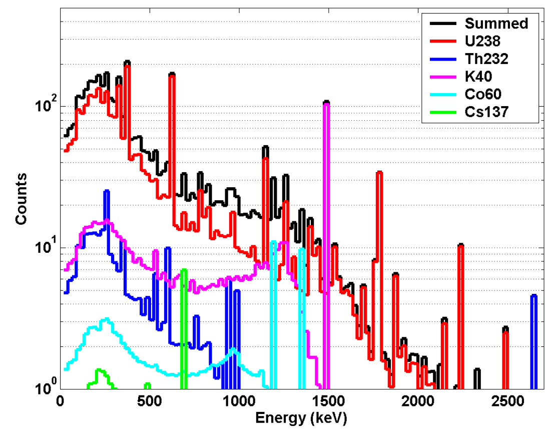

(b)

Figure 3-15. Poly data with background subtracted compared to simulation.
A) Background subtracted data from the poly sample compared to the Monte Carlo simulation.
B) Histograms of the various decays used to create the summed spectrum used in the left plot.

3.8 Teflon Arcs Used in the XENON10 Inner Detector

Since the innermost detector structure is composed of teflon it is vitally important to insure that the teflon used is very clean of radioactive impurities. Fortunately, it turns out that this teflon is a subdominant source of background. The activity of the sample was calculated to be

mBq/kg (15.0 / 5.54 / 60.69±24.12 / 1.67 / 1.21) (U /Th / K / Co / Cs)

Table 3-12 shows the numbers used to calculate the activity via the first analysis procedure discussed. The mass of this sample was 0.68 kg. Table 3-13 shows the numbers used to calculate the activities using the fitting method discussed above. Figure 3-18 shows the fit and the individual components. It appears that, just like the poly fit, the code overestimates the amount of ^{40}K present, as well as the amount of ^{238}U. This effect can be seen in both the numbers in Table 3-13 as well as the fitted simulations shown in Figure 3-18.

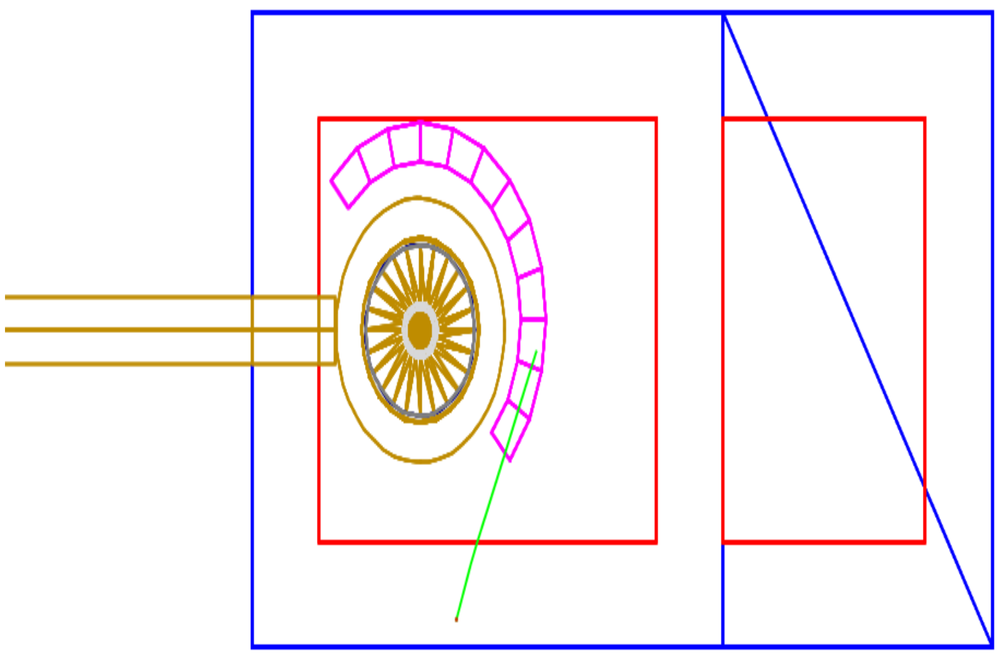

Figure 3-16. Teflon arc sample placement within the Monte Carlo simulation.

Table 3-12. Teflon sample activities using the background comparison method.

Line Energy (keV)	Bkg (cnts)	Data(cnts)	Efficiency	Activity (mBq/kg)
^{40}K (1460.8)	115	196	2.73e-4	60.69±24.12

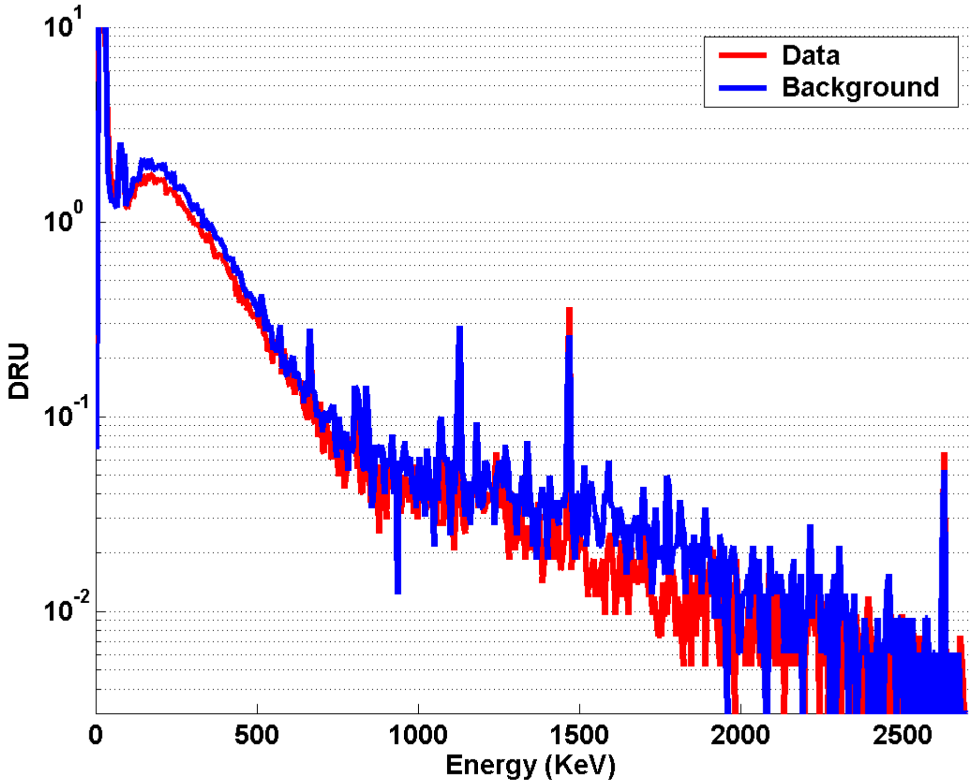

Figure 3-17. Teflon sample data and background data, normalized to DRU. The background used is the new background taken over 25.8511 days. The spectrum for the teflon sample was taken over 36.1403 days from 5-24-2006 to 7-10-2006 and 10-10-2006 to 11-2-2006. A DAQ failure during the first counting session necessitated the subsequent recount.

Table 3-13. Teflon sample activities using the fitting method.

Line	Scale Factor	Events Simulated	Activity (mBq/kg)
^{238}U	1.77e-5	1e6	15.0
^{232}Th	6.54e-6	1e6	5.5
^{40}K	2.52e-5	1e7	214
^{60}Co	1.98e-7	1e7	1.7
^{137}Cs	1.43e-7	1e7	1.2

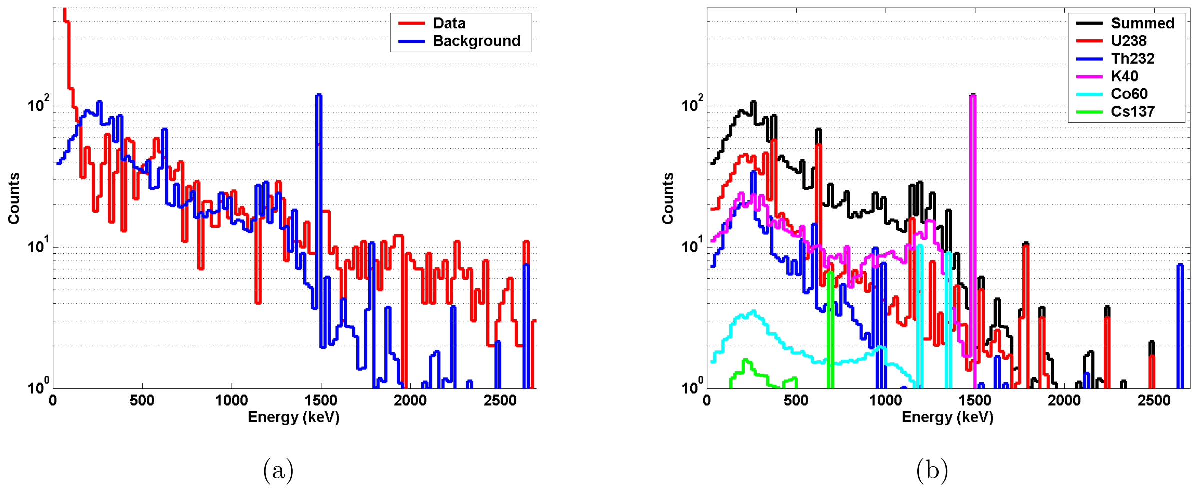

Figure 3-18. Teflon data with background subtracted compared to simulation.
A) Background subtracted data from the teflon sample compared to the Monte Carlo simulation.
B) Histograms of the various decays used to create the summed spectrum used in the left plot.

3.9 Sample Z: Stainless Steel and Ceramic Feedthroughs

To be confident in the activities of the various feedthroughs present, others besides the ceramic pieces screened previously by DIODE-M must also be measured. These two are the largest of the feedthrough samples provided, containing a stainless steel body with a ceramic center. The large activities determined via the fitting method yet not seen in the actual data as noticeable peaks is indicative of the results being dominated by low statistics. As such these samples will have to be re-screened at the LNGS where the improved background will aid in obtaining higher statistics. The activity of the sample was calculated to be

mBq/FT (55.6 / 0.28 / 157 / 9.12±1.48 / 9.33) (U /Th / K / Co / Cs)

Table 3-14 shows the numbers used to calculate the activity via the first analysis procedure discussed. The mass of the two feedthroughs is 0.654 kg. While ^{60}Co is obviously present, all of the other decays are however limited by statistics. Table 3-15 shows the numbers used to calculate the activities using the fitting method discussed above. Figure 3-21 shows the fit and the individual components.

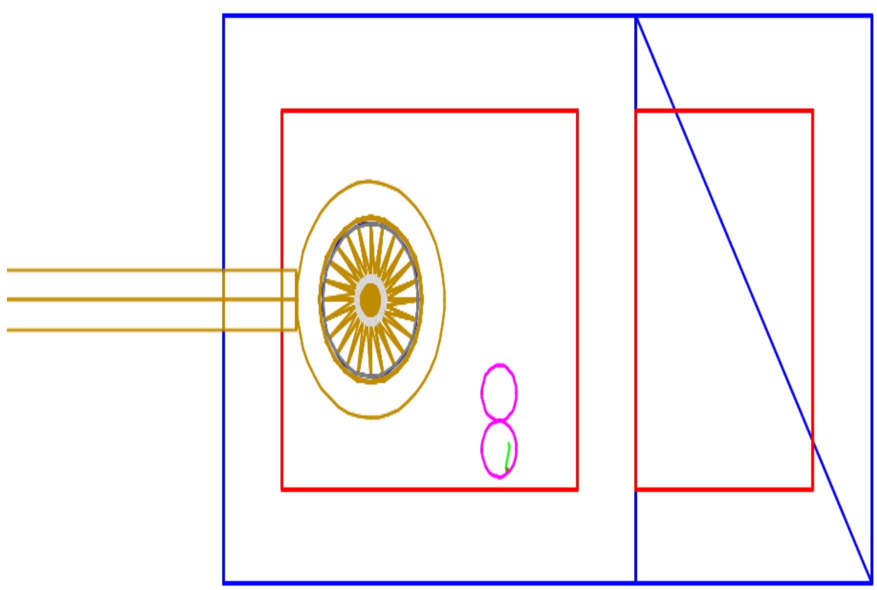

Figure 3-19. Sample Z placement within the Monte Carlo simulation.

Table 3-14. Sample Z, the two feedthroughs, activities using the background comparison method.

Line Energy (keV)	Bkg (cnts)	Data(cnts)	Efficiency	Activity (mBq/kg)
^{60}Co (1173.2)	29	78	1.65e-3	<1.51
^{60}Co (1332.5)	27	70	1.05e-3	<0.870

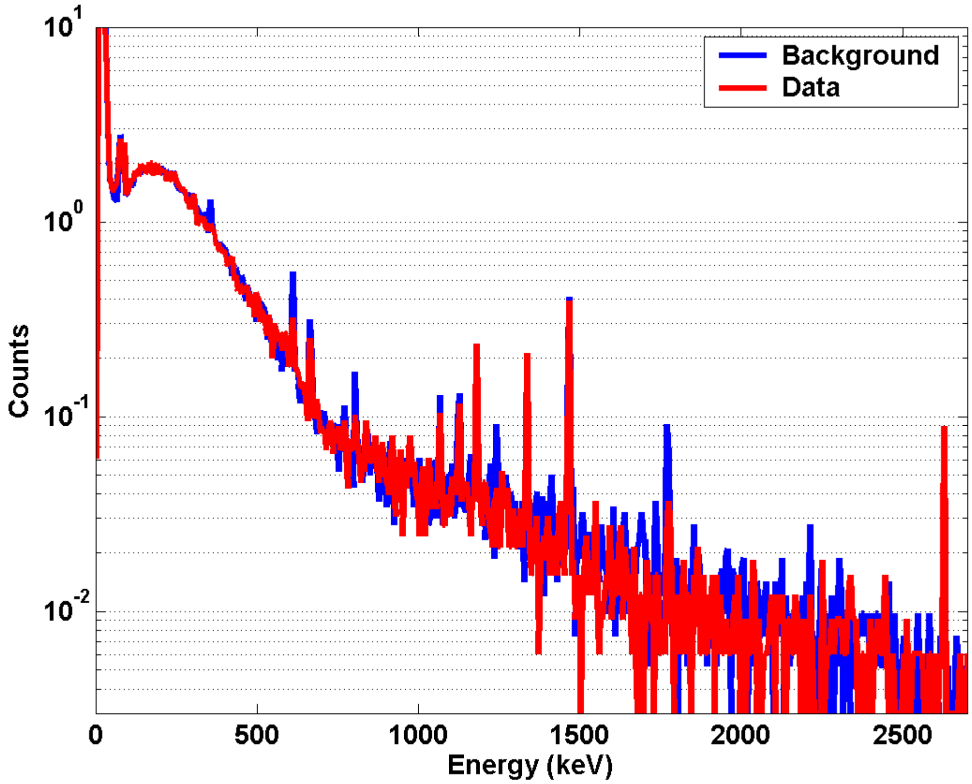

Figure 3-20. Sample Z data and background data, normalized to DRU. The background used is the latest background taken over 35.7063 days. The spectrum for sample Z was taken over 26.1378 days from approximately 2-23-2007 to 3-29-2007.

Table 3-15. Sample Z, the two feedthroughs, activities using the fitting method.

Line	Scale Factor	Events Simulated	Activity (mBq/kg)
^{238}U	1.95e-5	1e7	55.6
^{232}Th	9.70e-8	1e7	0.280
^{40}K	5.45e-5	1e7	157
^{60}Co	4.80e-7	1e7	1.38
^{137}Cs	3.24e-6	1e7	9.33

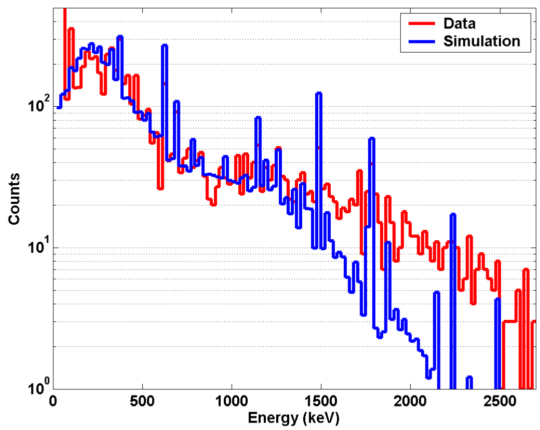

(a)

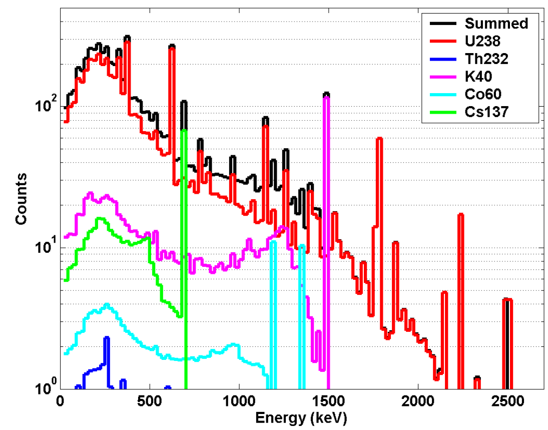

(b)

Figure 3-21. Feedthrough data with background subtracted compared to simulation.
A) Background subtracted data from sample Z compared to the Monte Carlo simulation.
B) Histograms of the various decays used to create the summed spectrum used in the left plot.

3.10 Sample H: Stainless Steel Used to Create the PMT Electrodes

As previously mentioned, Hamamatsu has provided many of the component materials used in the construction of their PMTs. The first of these samples measured was two sheets of the steel used to create the electrodes. The activities reported below are even more strongly dominated by low statistics than the feedthrough activities. This is a fairly low activity sample which will greatly benefit from a re-screening at LNGS. As such the calculated activities can not be trusted and only indicate the need for more data. The activity of the sample was calculated to be

mBq/kg (772 / 342 / 1070 / 12.1 / 2.90±6.24) (U /Th / K / Co / Cs)

Table 3-16 shows the numbers used to calculate the activity via the first analysis procedure discussed. The mass of the two sheets is 0.118 kg. Table 3-17 shows the numbers used to calculate the activities using the fitting method discussed above. Figure 3-25 shows the fit and the individual components.

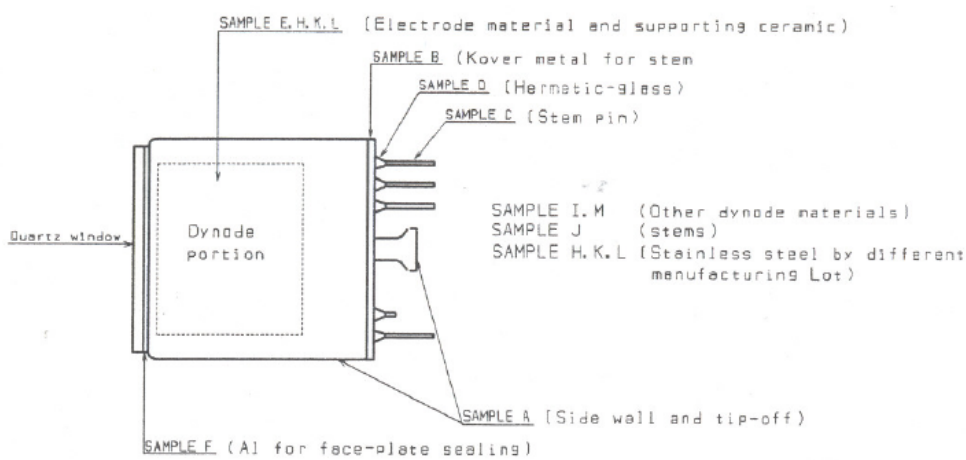

Figure 3-22. Breakdown of all of the PMT samples supplied by Hamamatsu. Sample H was screened in the SOLO facility, the remaining samples will be screened at LNGS.

Table 3-16. Electrode material sample activities using the background comparison method.

Line Energy (keV)	Bkg (cnts)	Data(cnts)	Efficiency	Activity (mBq/kg)
^{137}Cs (661.6)	95	180	8.53e-3	2.90±6.24

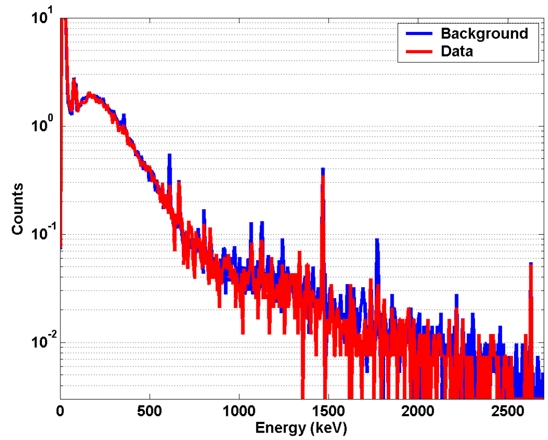

Figure 3-23. Sample H data and background data, normalized to DRU. The background used is the latest background taken over 35.7063 days. The spectrum for sample H was taken over 17.9465 days from approximately 3-29-2007 to 4-20-2007.

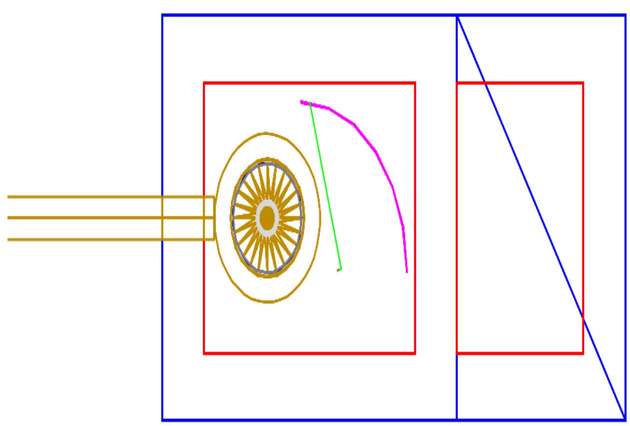

Figure 3-24. Sample H placement within the Monte Carlo simulation.

Table 3-17. Sample H, the electrode material sample, activities using the fitting method.

Line	Scale Factor	Events Simulated	Activity (mBq/kg)
^{238}U	1.58e-5	1e7	772
^{232}Th	7.00e-6	1e7	342
^{40}K	2.19e-5	1e7	1070
^{60}Co	2.48e-7	1e7	12.1
^{137}Cs	1.63e-7	1e7	7.99

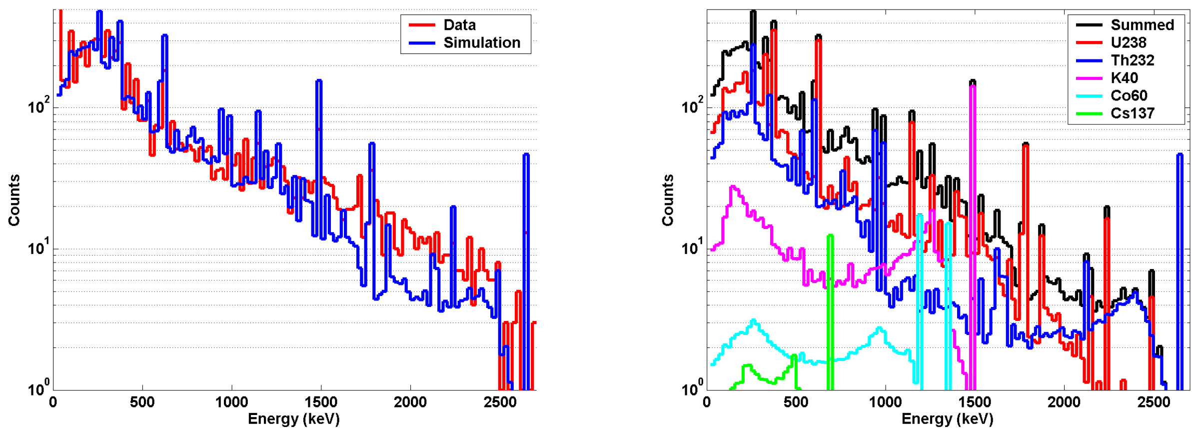

(a) (b)

Figure 3-25. Electrode material data with background subtracted compared to simulation. A) Background subtracted data from sample H compared to the Monte Carlo simulation.
B) Histograms of the various decays used to create the summed spectrum used in the left plot.

3.11 Summary of Screening Operation

The GATOR detector is a very powerful tool for the very accurate measurement of material activities. This material screening is a crucial step in the proper selection of materials for a next generation Dark Matter detector. Proper selection of materials can help ensure that the background of a new detector is as minimized as possible, which is a necessity in these types of low background experiments. However, certain ultra low background samples require a sensitivity that is difficult to reach with the GATOR located in the SOLO facility. The improved background observed at the LNGS installation will increase the GATOR detector's sensitivity, decreasing the time required to achieve satisfactory statistics for low activity samples. While currently some of the screened samples discussed in this Chapter are very clearly dominated by low statistics (the feedthroughs and the electrode material are the prime example), the new incarnation in Italy will be able to more accurately measure the activities of these samples.

CHAPTER 4
XENON10 BACKGROUND

4.1 The XENON10 Detector

The active Xenon volume is defined by a Teflon cylinder with an inner diameter of 20 cm and a height of 15 cm. Teflon was chosen due to it reflecting UV light (the scintillation light in liquid Xenon is at 182 nm) and as an electrical insulator. Teflon also has a very low intrinsic background which makes it ideal for the innermost detector material, not counting Xenon of course. Four stainless steel mesh grids are used to define the electric field within the liquid and gaseous Xenon. Two of these grids are within the liquid and two are within the gas with appropriate voltages to drift the electrons within the liquid, extract them to the gas and then accelerate them within the gas.

To detect the photons released from interactions in the liquid and gas, two arrays of 2.5 cm square photomultiplier tubes (PMTs) are placed on top and bottom of the detector volume. The bottom array of 41 PMTs is placed in the liquid below the cathode grid, and collects most of the direct light released during an interaction due to a strong reflection at the liquid gas interface. The top array of 49 PMTs is located in the gas and collects most of the proportional light released by the accelerating electrons through the gas.

The entire inner detector is encased in a stainless steel inner cryostat which itself is contained and vacuum insulated within a stainless steel outer cryostat. The total mass of these two stainless steel containers is roughly 180 kg and comprises the largest amount of material within the detector. A pulse tube refrigerator is used to reach and maintain the 180 Kelvin temperature required for Xenon liquification. Constant purification of the Xenon is achieved by circulating the Xenon out of the inner detector and through a high temperature getter.

To lower the number of background events seen the XENON10 detector is placed within the Gran Sasso mine (3100 meters water equivalent) thereby reducing the muon flux by a factor of 10^6 making a muon veto unnecessary. To combat stray neutrons a

20 cm polyethylene shield was placed around the detector. Surround the polyethylene is a further 20 cm of lead to reduce the flux of incoming gamma rays. However, even though much care is taken to reduce the intrinsic background of the detector, the shield materials and the detector materials will have some intrinsic radiation and these will need to be determined to better understand the data we receive. Current measurements indicate that the steel and the PMTs are the main contributors to the detector background.

Figure 4-1. Photograph of the XENON10 Detector and the shield that surrounds it.

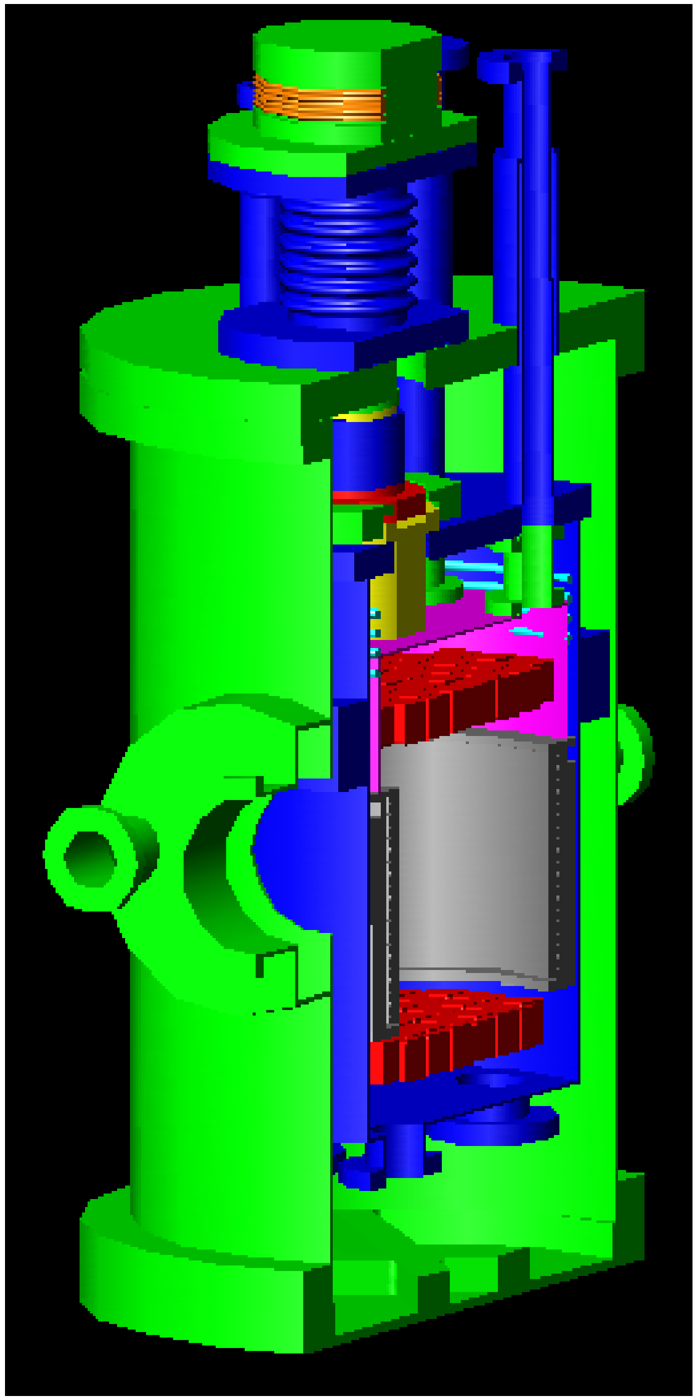

Figure 4-2. Cross-sectional drawing of the XENON10 Detector drawn using AutoCAD 2004. The outer green structure is the outer cryostat, the inner blue structure is the inner cryostat, the innermost grey structure is the teflon inner chamber. Also shown in red are the two PMT arrays.

4.2 Analysis of Individual Components

4.2.1 Monte Carlo Simulations for XENON10

The Monte Carlo simulation put together for the XENON10 detector was the combined work of several people within the XENON collaboration. Almost all of the components were added into the geometry based off of the mechanical drawings used to construct the detector. The inner and outer stainless steel cryostats were coded with as many of the flanges and connections as possible, based off of the drawings as well as photographs that show additional flanges not present in said drawings. Inside the cryostats, the teflon inner detector and PMT arrays were also created as accurately as possible. The wire grids within the Xenon were approximated as a thin steel disk with a reduced density so that the final mass of the grid is equal to the real mass. The poly and lead shields as well as the steel support structure outside of the cryostats are also present. Figure 4-3 shows a 3-dimensional cross-sectional drawing of the simulation, although due to the many components making out the finer details is understandably difficult. The various decays of interest are simulated originating from within a given geometrical

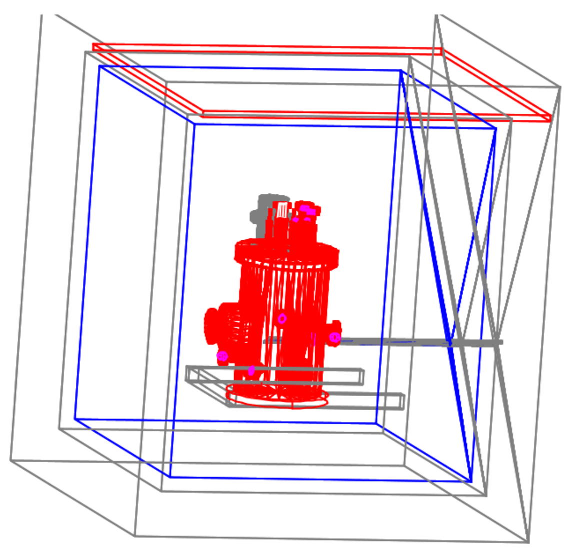

Figure 4-3. Cross-sectional image of the XENON10 simulation, showing primarily the shield and the outer cryostat.

volume and the energy deposition within the liquid Xenon is recorded. One thing that is of interest is an estimate on the number of background events that will be seen in the detector from a given material or decay. This estimate is carried out by plotting DRU versus energy and integrating. A typical simulation will yield counts versus energy so the Y-axis will have to be scaled appropriately, using Equation 4–1.

$$DRU(events \cdot kg^{-1} \cdot day^{-1} \cdot keV^{-1}) = \frac{Activity(Bq \cdot Unit^{-1}) \cdot UnitNumber \cdot 86400}{N \cdot M_{Xenon} \cdot BinWidth} \tag{4–1}$$

Where N is the number of events simulated, 86400 represents the number of seconds per day, $Bq \cdot Unit^{-1}$ is the activity as measured by GATOR in whatever units are required (Bq/kg, Bq/PMT et cetera), M_{Xenon} is the mass of the active Xenon target, $BinWidth$ is the width of each histogram bin in keV and $UnitNumber$ is the amount of whichever piece is being analyzed (inner cryostat mass, number of PMTs et cetera).

To increase the accuracy of this estimate, two data cuts will be implemented similar to the quality cuts done on the actual XENON10 data. The first is a simple fiducial volume (FV) cut. Most of the events will occur in the outer regions of the liquid Xenon, so by making a geometrical cut and only considering events that occur within the central regions, we can use this self-shielding to reduce the background by a substantial amount. This central region consists of a cylinder 160 mm in diameter and 93 mm tall for an approximate fiducial mass of 5.4 kg.[1]

The other cut uses the resolution of the detector to cut out multiple scatters since the probability of a WIMP undergoing multiple scatters in a detector of this size is vanishingly small. First all events that occur within a 150 μs window are grouped together as one event. This is mostly a required criteria for the Uranium and Thorium decay chains which have daughter decays with half-lives above 150 μs. Decays such as Cobalt and Potassium occur at one time and since the gamma rays travel at the speed of light, all depositions

[1] For comparison the full volume is 200 mm in diameter and 150 mm tall with an approximate total mass of 15 kg

will be seen at the same point in time. Once all of the depositions have been lumped together as one event, only events within 3 mm of each other in Z are considered to be a single scatter. Events with energy depositions further apart than 3 mm can be seen as a multiple scatter and discarded. Figure 4-4 shows the results from these successive cuts. The first cut applied is the fiducial volume cut (FV) while the multiple scatter cut (MSC) is applied second. The following subsections will detail the application of this method

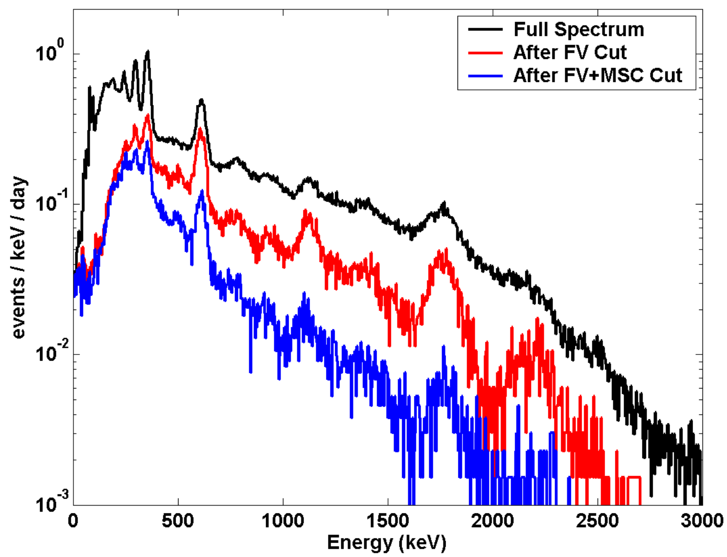

Figure 4-4. Example of successive cuts being applied to simulation data. This simulation represents the decay of Uranium-238 from within the Inner Cryostat. Note that the y-axis is scaled almost in DRU, missing only the sample mass and thus merely represents raw simulation data, not actual data. The black line is from all events with no cuts, the red line is the data after the Fiducial Volume cut and the blue line is the data after the Multiple Scatter cut as well.

to the majority of the detector components to approximate the background level within the detector. Each analysis utilizes the results from the material screening to generate the listed numbers, both for the full energy spectrum and the low energy region defined as 0 to 50 keV.

4.2.2 Outer Cryostat

The outer cryostat represents the largest structures in close proximity to the active Xenon volume. The high background values we would expect from this large mass of steel is moderated slightly by the intervening steel of the Inner Cryostat. Regardless, it is expected that a majority of the background will be due to the nearby stainless steel components. Future versions of the XENON detector will have to take this into account, either by replacing the steel with a cleaner material such as ultra-low background Copper, reducing the steel mass or some other such mechanism.

Table 4-1. 0-3000 keV Cryostat contribution to the detector background. The lower activity steel from Section 3.6 is assumed for this analysis.

Decay	No Cuts (mDRU)	FV Cut (mDRU)	MS Cut (mDRU)
^{60}Co	216	65	17
^{137}Cs	73	14	4
^{40}K	209	59	15
^{232}Th	1426	308	81
^{238}U	365	75	20
Total	2288	521	137

Table 4-2. 0-50 keV Outer Cryostat contribution to the detector background.

Decay	No Cuts (mDRU)	FV Cut (mDRU)	MS Cut (mDRU)
^{60}Co	56	15	13
^{137}Cs	19	4	3
^{40}K	61	12	11
^{232}Th	348	74	66
^{238}U	94	17	15
Total	578	121	109

4.2.3 Inner Cryostat

The Inner Cryostat, while only roughly a quarter the mass of the Outer Cryostat, has almost no shielding between the steel and the active Xenon volume. Thus if the steel that comprises the Inner Cryostat has an appreciable activity it will definitely have a noticeable effect on the background. Given the lack of shielding, it is even more important that future renditions of the detector take special care with the Inner Cryostat to insure the lowest background possible.

4.2.4 PMTs and Bases

The PMTs and the associated cirlex bases reside within the Xenon itself making it vitally important that these be of the lowest activity possible. Current estimates indicate

Table 4-3. 0 - 3000 keV Inner Cryostat contribution to the detector background. The lower activity steel from Section 3.6 is assumed for this analysis.

Decay	No Cuts (mDRU)	FV Cut (mDRU)	MS Cut (mDRU)
^{60}Co	278	101	27
^{137}Cs	124	25	7
^{40}K	409	91	27
^{232}Th	1841	485	126
^{238}U	518	124	34
Total	3170	826	221

Table 4-4. 0 - 50 keV Inner Cryostat contribution to the detector background.

Decay	No Cuts (mDRU)	FV Cut (mDRU)	MS Cut (mDRU)
^{60}Co	39	26	22
^{137}Cs	30	8	7
^{40}K	176	12	11
^{232}Th	241	120	103
^{238}U	77	33	30
Total	562	197	174

that the PMTs are one of the dominant sources of background radiation, implying that the steel used in the XENON10 detector may be of a lower activity than the UF steel that was screened by GATOR. The numbers in Table 4-5 are dominant in comparison to those in Table 4-7 or Table 4-9 however they are much lower than the Cryostat numbers. The aforementioned screening of the PMT components that is planned for the LNGS GATOR detector will be very important in aiding Hamamatsu in constructing lower activity PMTs and reducing a dominant source of background radiation.

The PMTs and bases are simulated as a single unit in the Monte Carlo simulation. For the analysis the activities of the two components are added together.

Table 4-5. 0 - 3000 keVPMT and cirlex PMT base contribution to the detector background.

Decay	No Cuts (mDRU)	FV Cut (mDRU)	MS Cut (mDRU)
^{60}Co	0.3	0.2	0.04
^{137}Cs	0.1	0.05	0.01
^{40}K	2.2	0.5	0.1
^{232}Th	1.6	0.8	0.2
^{238}U	2.3	1.0	0.3
Total	6.4	2.5	0.7

Table 4-6. 0 - 50 keV PMT and cirlex PMT base contribution to the detector background.

Decay	No Cuts (mDRU)	FV Cut (mDRU)	MS Cut (mDRU)
^{60}Co	0.07	0.03	0.03
^{137}Cs	0.07	0.02	0.01
^{40}K	5.7	0.1	0.1
^{232}Th	0.7	0.2	0.2
^{238}U	1.5	0.2	0.2
Total	8.1	0.6	0.5

Table 4-7. 0 - 3000 keV Teflon contribution to the detector background.

Decay	No Cuts (μDRU)	FV Cut (μDRU)	MS Cut (μDRU)
^{60}Co	16	11	3
^{137}Cs	9	3	1
^{40}K	73	23	6
^{232}Th	61	34	8
^{238}U	168	81	20
Total	327	152	38

Table 4-8. 0 - 50 keV Teflon contribution to the detector background.

Decay	No Cuts (μDRU)	FV Cut (μDRU)	MS Cut (μDRU)
^{60}Co	2	2	2
^{137}Cs	7	1	0.8
^{40}K	82	4	3
^{232}Th	11	8	7
^{238}U	36	18	16
Total	139	33	29

4.2.5 Teflon

The Teflon Inner Detector defines the liquid Xenon volume, thus again there is no shielding to block any radiation. Unlike the PMTs however, Teflon is very easy to obtain in a very clean form. Additionally, the Teflon structure plays several very important roles and is basically irreplaceable so again it becomes important to minimize the background however possible. In the case of Teflon, future designs will not be able to replace the material and will instead have to rely on obtaining the cleanest Teflon available. The numbers shown Table 4-7 indicate that the background contribution from Teflon is subdominant and as long as appropriate care is taken in the selection and manufacture of future Teflon pieces the background contribution should remain subdominant for future incarnations.

4.2.6 Poly Shield

The polyethylene shield surrounding the XENON10 detector is the second most massive piece of the detector, the first being the Lead shield. Fortunately the poly is shielded from the active Xenon by two layers of stainless steel which should moderate any activity by an appreciable amount. Additionally, "clean" poly is relatively easy to obtain. As expected, the background contributions, shown in Table refPolytable, will be far below other contributions. The values seen here indicate that the current poly shield in use should suffice, assuming it is large enough, for future detectors.

Table 4-9. 0 - 3000 keV Poly shield contribution to the detector background.

Decay	No Cuts (μDRU)	FV Cut (μDRU)	MS Cut (μDRU)
^{60}Co	21	5	1
^{137}Cs	5	0.7	0.2
^{40}K	57	14	4
^{232}Th	51	9	3
^{238}U	358	63	17
Total	490	92	25

Table 4-10. 0 - 50 keV Poly shield contribution to the detector background.

Decay	No Cuts (μDRU)	FV Cut (μDRU)	MS Cut (μDRU)
^{60}Co	5	1	1
^{137}Cs	1	0.1	0.1
^{40}K	17	5	4
^{232}Th	12	3	2
^{238}U	87	14	13
Total	123	23	20

4.3 Comparison of Simulations to Data

Another important analysis to consider is comparing these simulations to the actual XENON10 background data. Several people within the collaboration have been making an effort to compare simulations ranging from simplistic models using nothing but cylinders to the more complex model previously discussed that attempts to emulate the actual detector as closely as possible. Such comparisons try to approximate the actual data collection techniques and analysis cuts and use the screening values as a starting point for fitting the simulations to the data. The prior analysis also indicates which samples should be dominating the background, providing an idea which activities to scale to best fit the data. Other sample activities have been obtained from Brown's screening operation from the DIODE-M detector operated at SOLO and almost every detector volume is approximated.

Figure 4-6 shows the results of one such set of simulations completed using the aforementioned full simulation. The main activities included in this comparison are the PMTs (with bases included), the Inner and Outer Cryostat, the Poly shield, three sets of Feedthroughs and Kr^{85} decay within the liquid Xenon.[2] Using the screening values will provide a starting point with which to begin the fit, as shown in Figure 4-5.

[2] The feedthroughs are metal and ceramic pieces that allow electronic connections to be made through the cryostats. A set of 3 is in the bottom of the inner cryostat, 4 are located in the side of the outer cryostat and 4 are located in the top of the outer cryostat.

Using the same fitting program used in the GATOR sample analysis presented in Chapter 3, the 41 histograms used to generate Figure 4-5 were varied and cycled over to generate the starting fits. This initial fitting, done from 1 to 750 keV, led to unreasonable results. Specifically the activities as determined by the fit for the PMTs and the Teflon were amazingly high when it has been well established that these components are fairly clean. To compensate for this and thereby produce a more realistic fit, several changes were made to the fitting code. The PMTs and Teflon were removed from the fitting rotation and their starting values maintained throughout the process. Additionally, almost all of the PMTs located in the XENON10 detector were screened by a separate screening operation within the collaboration and the results used to create a more accurate average PMT activity (listed below in Table 4-11). Furthermore, the 15 histograms that make up the three feedthrough simulations were locked together such that the different sets of feedthroughs will have the same activities throughout the fitting process. Taking all of this into consideration, the starting activities for the fit shown in Figure 4-5 are shown in Table 4-11.

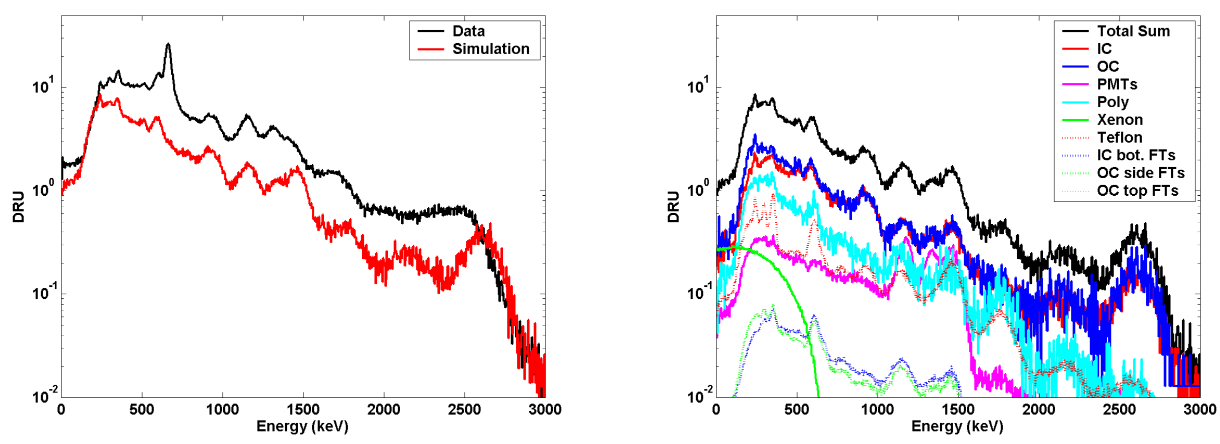

(a) (b)

Figure 4-5. Initial simulation scaling using the screening values from GATOR and DIODE-M.
A) The summed spectrum compared to the actual Xenon10 data.
B) The breakdown of the various histograms used to create the summed histogram.

Table 4-11. Initial activities used prior to the running the fitting program, acting as starting values for to code.

Sample	Activity (U / Th / K / Co / Cs) (mBq / unit)
IC and OC	13.43 / 44.07 / 116.94 / 7.30 / 5.98
PMTs	0.145 / 0.136 / 8.29 / 1.68 / 0.0367
Teflon	15 / 5.54 / 60.7 / 1.67 / 1.21
Poly Shield	22.3 / 25.3 / 53.2 / 1.06 / 0.663
Feedthroughs	55.6 / 0.28 / 157 / 9.12 / 9.33
Xenon	2.52

The fitting program was operated from 1 to 750 keV, which covers the main areas of interest, including the low energy region, several Uranium and Thorium peaks and the very prominent Cesium peak. Figure 4-6 shows this final fit while Figure 4-7 shows the individual histograms used in the comparison. Exactly as presented in Chapter 3, the scaling factors used to create the shown fit can be transformed into an activity for the various samples, the results of which are shown in Table 4-12, recalling that the PMT and Teflon activities were not allowed to change during this process. All of the activities determined by this method are within the bounds of believability. As expected the Steel from the Inner and Outer Cryostats comprises the main bulk of the activity and the Feedthroughs seem particularly active while the Poly Shield doesn't appear to contribute much to the background. Since the main features and contaminants are reasonably understood with this kind of information, informed decisions regarding material selection and detector design can be made for the next phase of the XENON experiment, XENON100 (note that these decisions will be discussed in Chapter 6).

Table 4-12. Final activity values as determined by fitting the simulations to data.

Sample	Activity (U / Th / K / Co / Cs) (mBq / unit)
IC	3.31 / 128 / 159 / 125 / 269
OC	0.041 / 0.085 / 9.48 / 125
PMTs	0.145 / 0.136 / 8.29 / 1.68 / 0.0367
Teflon	15 / 5.54 / 60.7 / 1.67 / 1.21
Poly Shield	0.067 / 0.073 / 0.096 / 0.068 / 0.090
Feedthroughs	6.1 / 1.27e-3 / 1107 / 53.8 / 359
Xenon	1.02e-4

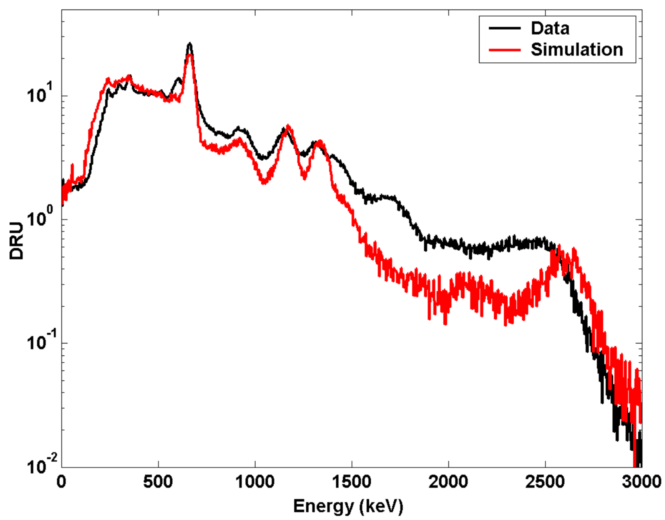

Figure 4-6. Comparison of a background simulation to data, including all of the samples screened by GATOR as well as several samples screened by the DIODE-M detector operated by the Xenon group at Brown and the PMT screening operation run by another collaborator in LNGS.

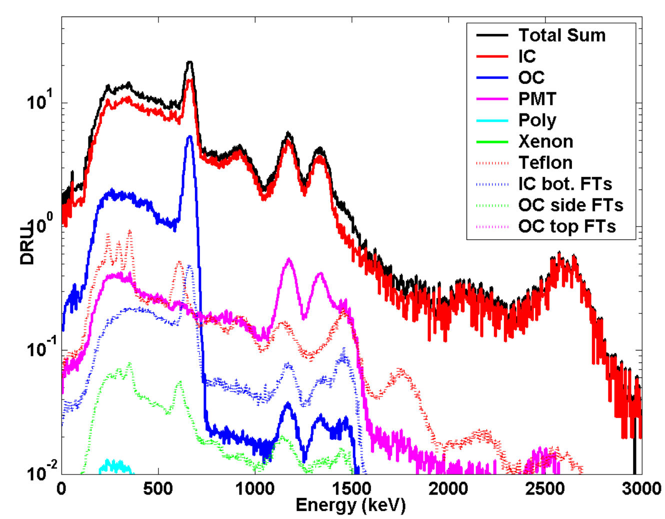

Figure 4-7. Breakdown of the Monte Carlo Simulation that was fit to the data, showing the individual sample histogram breakdowns as well as the summed spectrum that is shown in comparison with a data spectrum in Figure 4-6.

CHAPTER 5
FURTHER WORK FOR XENON

5.1 The UF XENON Prototype

The prototype detector briefly operated at UF, Aachen and now Zurich is in effect a smaller version of that searching for dark matter in Italy. The original purpose of this small prototype was to study the response to neutrons. Located in the basement of the UF Physics Building is a small proton accelerator that can be focussed onto a sample known to generate monoenergetic neutrons, thereby creating a neutron beam that can be sent towards the detector. A neutron detector was also obtained that can be placed at various angles around the detector with respect to the neutron beam. Coincidence between an event in the prototype detector and the neutron detector would indicate the angle of the nuclear recoil which, coupled with the energy of the beam would determine the energy of the recoil. As the desire is to have the information from this experiment apply to the larger detector, all of the main detector features must be included in the smaller prototype. It is unfortunate that this detector was relocated to Aachen before this experiment could be successfully completed.

The inner detector volume is defined by a teflon structure that creates a Xenon volume 2.3" square by 1.8" high. The entire teflon structure is contained within a 6" stainless steel can that has been electro-polished for purity reasons. This inner cryostat is termed the Ultra-High Vacuum (UHV) can. Surrounding the UHV can is a thin Aluminum tube, called the radiation can, designed to block thermal radiation from the outer cryostat can. The outermost can, termed the outer cryostat can, is a 10" diameter stainless steel shell that serves as the outer limits of the vacuum chamber.

All of the connections from outside to the inner portions of the detector; wiring, gas flow, vacuum, and a liquid Nitrogen cooling loop, are attached to the radiation can come through the outer cryostat top flange. The cold stick which provides the cooling power is connected through the bottom of the outer cryostat to the radiation can. Four of the

(a) (b)

Figure 5-1. Some views of the UF XENON Prototype.
A)The Inner Cryostat can, still attached to the Outer Cryostat top flange can be seen here resting on the table.
B) The entire Outer Cryostat can is shown within its supporting frame and resting on top of the liquid nitrogen dewar. Not shown is the cold finger which penetrates down into the liquid, providing the cooling power necessary to maintain liquid Xenon temperatures.

square PMTs view the detector volume from above, 2 of which can be seen in the sideview drawing of Figure 5-1.

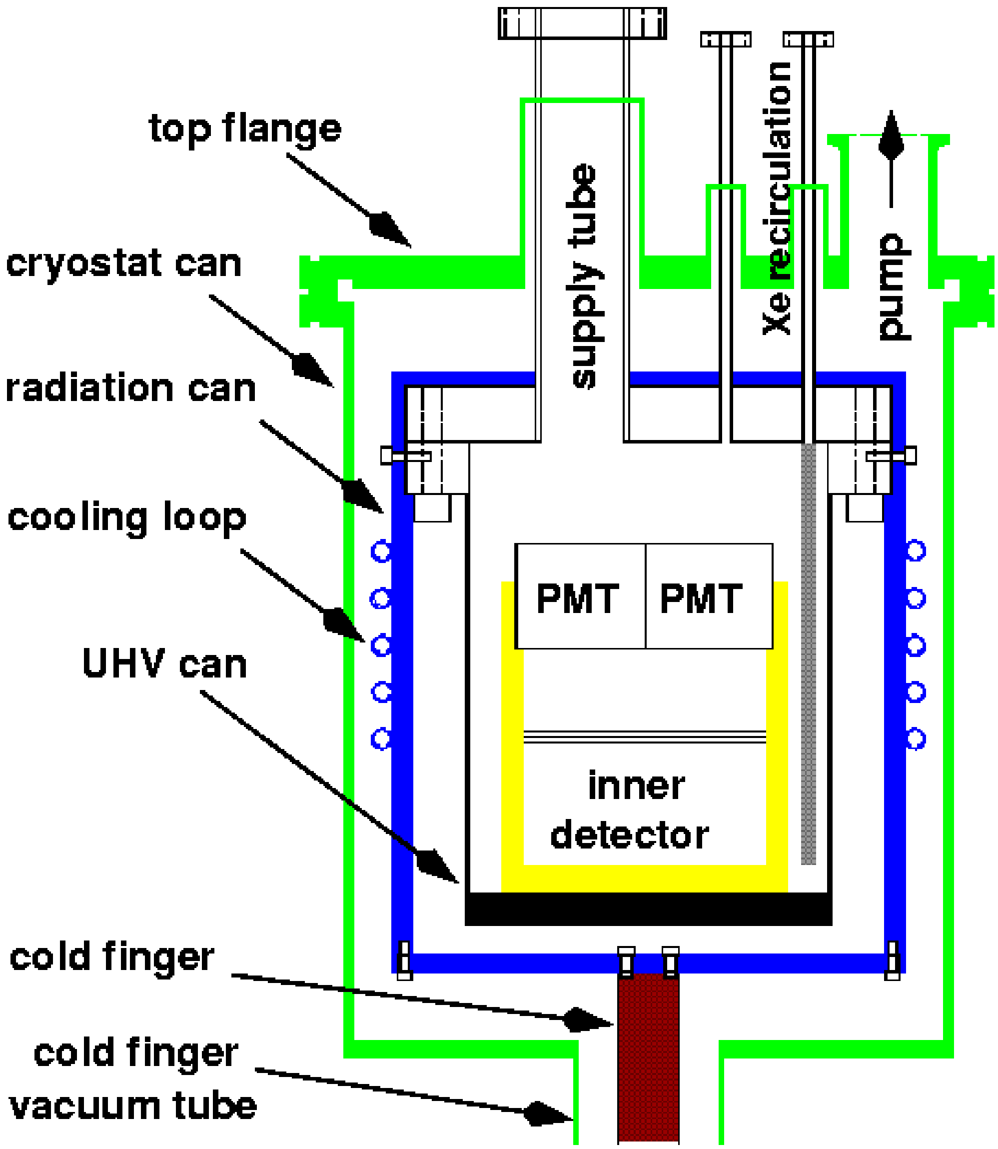

Figure 5-2. Side view of the UF XENON Prototype. Shown in green is the Outer Cryostat, in blue the Inner Cryostat, in yellow the Inner Detector and in brown the Cold Finger.

5.2 Gas System for UF XENON Prototype

The gas system at UF for the aforementioned prototype is similar in design to the one originally in operation at Columbia for the 3 kg Xe-Baby detector. Xenon costs an appreciable amount so it is important to maintain a storage and delivery system for the gas. Two four-gallon cylinders from Hoke are used to store the Xenon supply when not in use. The Xenon is trapped in these cylinders initially by submerging them in liquid Nitrogen. Once trapped, the Xenon is kept in one of the cylinders at approximately 1500 PSI. The majority of the rest of the gas system is designed to deliver the Xenon into the detector.

At the beginning of normal operating conditions, Xenon flows from one of the cylinders, through a pressure regulator which brings the pressure down from the 1500 PSI to roughly 40 PSI. It will then flow through the getter for purification, through a metering valve used to more accurately control the flow rate, and through a gauge to monitor the flow before heading out to the chamber.

During a typical data run, Xenon will flow with the aid of a diaphragm pump from the bottom of the inner chamber, through the getter to be repurified, and back out to the chamber. The gas system also has extra connections to allow for the initial high pressure transfer of Xenon after it was shipped to UF, a spark purifier, a vacuum pump, and an argon flush. The spark purifier is currently not being used nor is there a plan for one to be used. The argon flush also will be rarely used, allowing a positive pressure to be placed on the system when it is open, hindering the flow of water and other impurities into the chamber. The line to the vacuum pump only needs to be used when evacuating all of the tubing which should only be necessary when the system was initially created.

At the end of a run, Xenon can be returned to the cylinders via a direct high pressure line or recirculated through the getter. All of the 1/4" tubing, fittings, and valves were purchased from Swagelok. The getter is a SAES Mono Torr Heated Getter, designed for Argon, Helium and other rare gasses, which includes Xenon. It's designed to remove H_20,

O_2, H_2, CO, CO_2, N_2, THC and other particles to generally below 1 ppb. As the gas passes through the heated getter material, impurities are irreversibly trapped within the material and not released during changes in pressure or temperature.[27]

The Aluminum frame was built by the UF Physics Machine Shop and based off of a design for a balloon based gas system operated from Columbia. The valves are mounted to a thin aluminum plate on the attached to the front of the frame. All of the 1/4” stainless steel, electro polished tubing was bent and cut by hand using standard pipe hand tools. To deal with separate motions of the gas system and the detector during any transport, all connections from the side of the gas system to any external object are done via high pressure 3 foot long flex tubes. Differences in Japanese pipe fittings and British pipe fittings forced us to weld two of these fittings into the diaphragm pump.

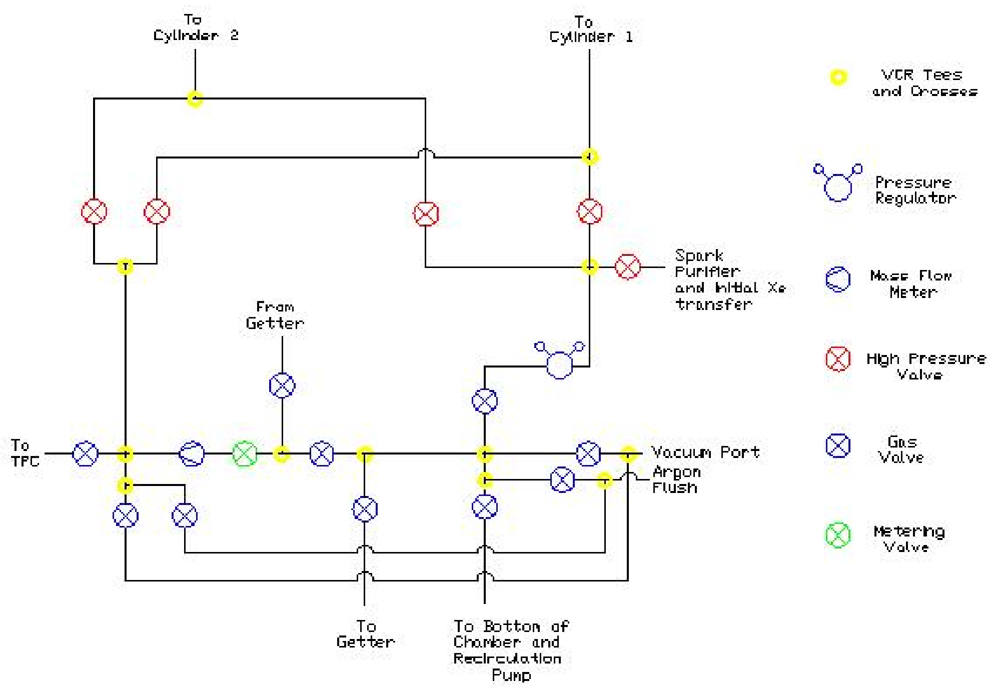

Figure 5-3. Gas System schematic, showing all tubing connections including all valves, storage cylinders, the UF XENON Detector, and all optional external connections.

Figure 5-4. Early image of the gas system front panel. The blue object on the bottom is the getter. Not shown are the two mass readouts for the storage cylinders on top, the flow meter in the left hand hole and the black lines indicating tubing connections between valves.

5.3 Electric Field Simulations for UF XENON Prototype

Before the UF Prototype was put into operation the electric field that we would expect within the detector was modeled. While we were confident that the applied voltages would create the field values that were desired, it was unclear if problems could arise due to these voltages. Sharp corners, the liquid Xenon circulation tube, the high voltage wires and proper electron capture were all issues that were in question. Of the issues in question, only the recirculation tube was believed to be of a concern. This stainless steel tube is at ground and lies very close to the steel grid structures. To insure arcing does not occur within the chamber, a thin teflon sheath was created to go around the tube. The simulations shown here already include this teflon cover, see the left portion of both Figure 5-6(a) and Figure 5-6(b) to see the strong field value that caused this concern.

These electric field simulations were created in Ansoft's Maxwell Student Version, available for download from www.ansoft.com. Further analysis was done using Garfield provided by Rob Veenhof at CERN, see consult.cern.ch/writeup/garfield/ to simulate the movement of electrons within the liquid.

The simulations seem to suggest that for the original 3-grid design, almost all of the electrons are collected at the anode, while a simple expansion to a 4-grid design insures that all of the electrons are collected at the anode. Adding in the electric field due to the PMTs achieves the same effect as the 4-grid design, suggesting that the current 3-grid design plus PMTs will be sufficient. The simulations used the following voltages:

- -3175V on the Cathode in both simulations and the Top Grid in the 4-grid simulation
- -1587.5V on the Bottom Grid in both cases and
- 0V on the Anode, the Inner Can, and the Recirculation Tube in both cases.

These potentials create a 5kV/cm drift field between the Anode and both the Top Grid (only in 4-grid simulation) and the Bottom Grid, and a little less than 1kV/cm drift field between the Cathode and the Bottom Grid. In vacuum, the drift field would be 1kV/cm, but the presence of the liquid Xenon lowers this value by a small amount.

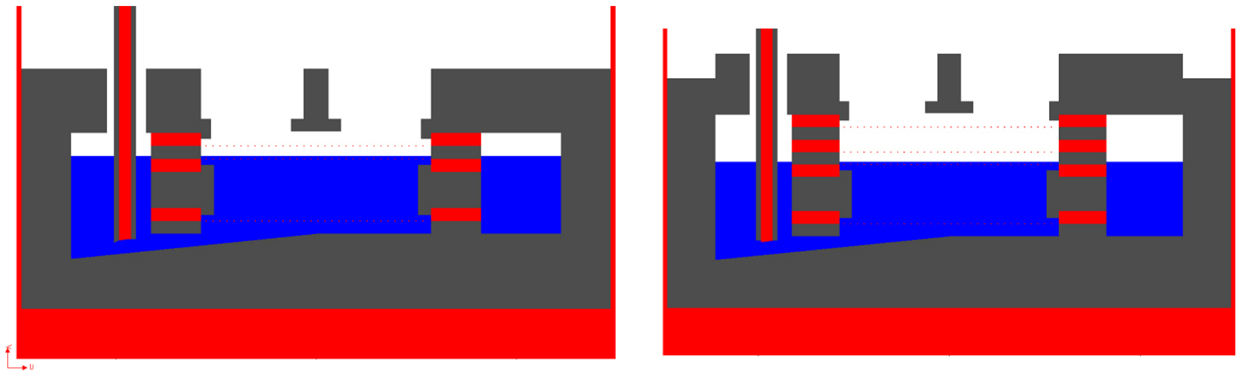

(a) (b)

Figure 5-5. Geometrical layout of the electric field simulation. ed structures are stainless steel, grey structures are teflon, the blue is liquid Xenon and the background is vacuum.
A) Three grid geometry.
B) Four grid geometry.

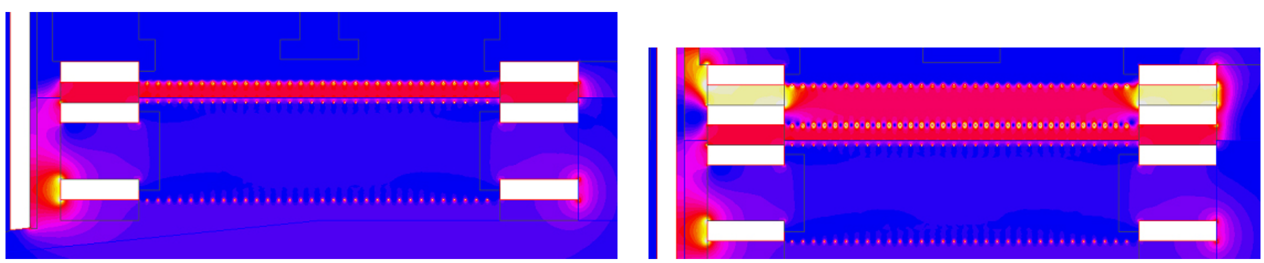

(a) (b)

Figure 5-6. Electric field plots within the inner detector. The coloring is a temperature based scheme, so blue represents lower values and red higher values of the electric field. For an idea of the scale, the field in the lower part of the detector is 1 kV/cm and in the top part of the detector is 5 kV/cm.
A) Three grid geometry.
B) Four grid geometry.

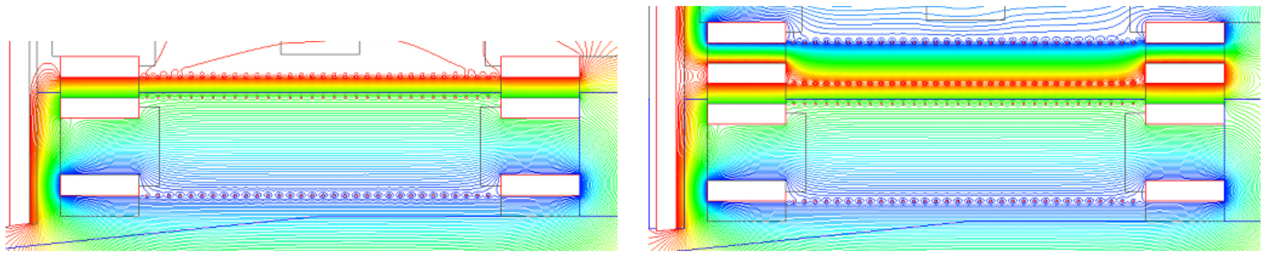

(a) (b)

Figure 5-7. Electric potential plots within the inner detector. What should be noted is how straight and parallel the potential lines are within the drift region, indicating a fairly uniform electric field.
A) Three grid geometry.
B) Four grid geometry.

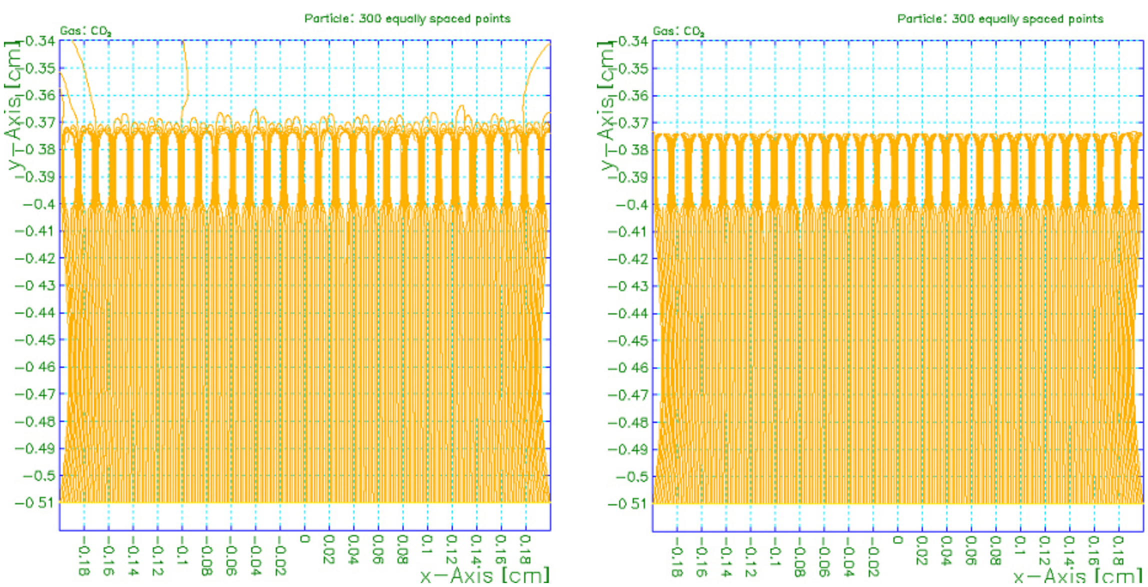

(a) (b)

Figure 5-8. Simulated electron drift tracks through the liquid Xenon. The electrons were created with zero velocity near the bottom of the chamber. In the three grid design only a small percentage of electrons escape past the anode while in the four grid design all electrons are captured at the anode.
A) Three grid geometry.
B) Four grid geometry.

CHAPTER 6
CONCLUSIONS

f The XENON collaboration announced the results from the operation of the Xenon10 detector at the April meeting of the American Physical Society. At that time and further at the time of the writing of this paper, the limit set by the Xenon10 detector for the WIMP mass (see Figure 1-4) was the best in the world[24]. However, so far only upper limits to WIMP-nucleon cross sections can be given, thus improvements to the design and size of the detector are key to further push the limits of the field. As the detector design changes to increase the fiducial mass, the opportunity exists to improve the background of the detector. One of the key improvements that can be made for a larger detector is constructed is to improve the background via a more careful selection of materials.

Thus the importance of the Gator detector and its screening operation. Understanding where the primary sources of background arise from can make it possible to remove them or at the very least minimize them for future detectors. The screening done with the Gator detector has helped show things such as the teflon being low enough in activity to be in the inner detector, that the steel is one of the largest contributors to the background, and future screenings will hopefully reveal what portion of the PMTs contributes most to the background allowing Hamamtsu to design and create lower activity PMTs for future experiments. These PMT screenings will occur during the operation of XENON100 and will allow for the creation of vastly superior PMTs by the time the scaling up to XENON1T is underway.

XENON100 is already in construction and planned to start taking data in the Spring of 2008 and is expected to improve the limit set by XENON10 by at least an order of magnitude. The design of the cryostat was made in such a way so as to reduce the steel mass below that of the XENON10 detector (down to approximately 60 kg in total compared to the 180 kg stainless steel cryostat system implemented in XENON10). Additionally an ultra-pure steel has been selected to be used in the XENON100 detector which should further help to reduce the background. Hamamatsu has designed lower background PMTs for this detector as well that are promised to be superior to those used in XENON10. Fundamental design changes have also been implemented such as relocating the feedthroughs and Pulse Tube Refrigerator (PTR) outside of the Lead shield[1] . It has also been decided to construct the XENON100 Inner Detector from an ultra low background Teflon using a custom designed mold built specifically for this application. All of these modifications and design decisions would not be possible without an advanced material screening operation like that done with the GATOR detector.

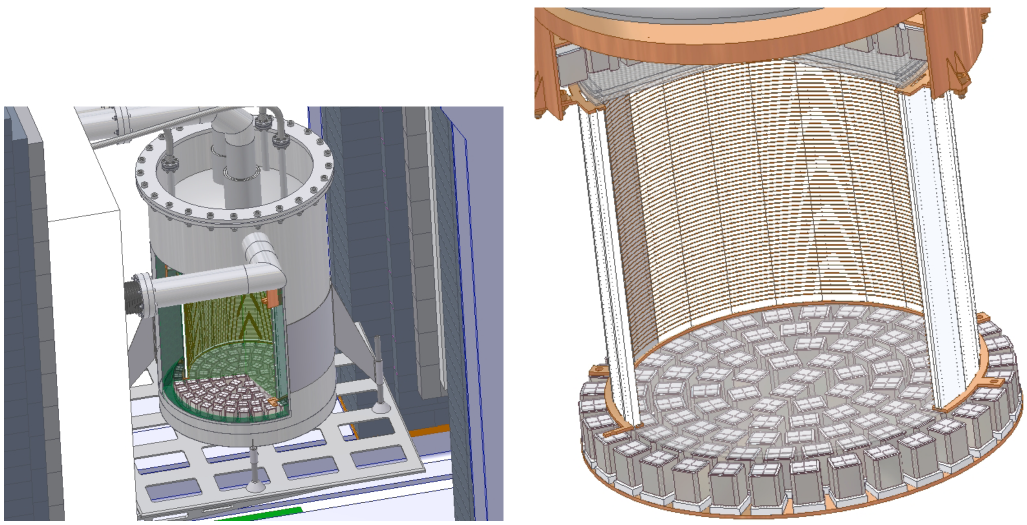

(a) (b)

Figure 6-1. Artistic renditions of the XENON100 Detector.
A) Graphic of the XENON100 Outer Cryostat placed in the current XENON10 shield, with a cut out showing the Inner Detector.
B) Image of the XENON100 Inner Detector, showing the PMT arrays, the Teflon structure, and the field shaping rings. The approximate size of the full Xenon volume will have a 15 cm radius and a 15 cm drift length. Images courtesy of Laura Baudis.

[1] The screening for these items was done by DIODE-M operated by Brown University, not GATOR. However the goals and methods of these separate screening operations are identical and the different detectors are operated in parallel.

REFERENCES

[1] Bradley W. Carroll and Dale A. Ostlie, "An Introduction to Modern Astrophysics", *Addison-Wesley*, New York, (1996).

[2] F. Zwicky, "On the Masses of Nebulae and of Clusters of Nebulae", *Astrophysical Journal*, **86**, 217, (1937).

[3] S.M. Faber and J.S. Gallagher, "Masses and Mass-to-Light Ratios of Galaxies", *Annual Reviews*, **17**, 135-187, (1979).

[4] V. Rubin, "Rotation of the Andromeda Nebula from a Spectroscopic Survey of Emission Regions", *Astrophysical Journal*, **159**, 379, (1970).

[5] M. Persic, P. Salucci and F. Stel, "The Universal Rotation Curve of Spiral Galaxies: I. The Dark Matter Connection", *Mon.Not.Roy.Astron.Soc.*, **281**, 27, (1996).

[6] G. Bertone *et al*, "Particle Dark Matter: Evidence, Candidates and Constraints", *Astrophysical Journal*, **405**, 279-390, (2005).

[7] G. Jungman *et al*, "Supersymmetric Dark Matter", *Physics Report*, **267**, 195-373, (1996).

[8] D.N. Spergel *et al*, "Wilkinson Microwave Anisotropy Probe (WMAP) Three Year Results: Implications for Cosmology", *Astrophysical Journal*, **170**, 377, (2007).

[9] D. Clowe *et al*, "A Direct Empirical Proof of the Existence of Dark Matter", *Astrophysical Journal*, **arXiv:astro-ph/0608407v1**, (2006).

[10] J. Primack, "Dark Matter and Structure Formation in the Universe", *Astrophysical Journal*, **arXiv:astro-ph/9707285v2**, (2007).

[11] Andrey Kravtsov, "Center for Cosmological Physics", *http://cosmicweb.uchicago.edu/index.html*, (2007).

[12] M. Davis *et al*, "The Evolution of Large-Scale Structure in a Universe Dominated by Cold Dark Matter", *Astrophysical Journal*, **292**, 371-394, (1985).

[13] R. Minchin *et al*, "A Dark Hydrogen Cloud in the Virgo Cluster", *Astrophysical Journal*, **622**, L21, (2005).

[14] J. Fukumoto, "Relative Abundances of Galaxies, Intracluster Gas, and Dark Matter in X-ray Clusters of Galaxies", *PASJ: Publications of the Astronomical Society of Japan*, **44**, L235-L240, (1992).

[15] C. Alcock *et al*, "The MACHO Project: Microlensing Results from 5.7 Years of LMC Observations", *The Astrophysical Journal*, **542**, 281, (2000).

[16] Arnon Dar, "Dark Matter and Big Bang Nucleosynthesis", *Astrophysical Journal*, **449**, 550, (1995).

[17] P. Tisserand *et al*, “Limits on the Macho Content of the Galactic Halo from the EROS-2 Survey of the Magellanic Clouds”, *Astrophysical Journal*, **469**, 387-404, (2007).

[18] L. Duffy *et al*, “A High Resolution Search for Dark-Matter Axions”, *Astrophysical Journal*, **arXiv:astro-ph/0603108**, (2006).

[19] L. Duffy, “High Resolution Search for Dark Matter Axions in Milky Way Halo Substruture”, University of Florida PhD Thesis, (2006).

[20] T.C. Yang , “Gauge Chiral U (1) Symmetry and CP Invariance in the Presence of Instantons”, *Physics Review Letters*, **41**, 523-526, (1978).

[21] B.R. Martin & G. Shaw, “Particle Physics”, *Wiley*, New York, (1997).

[22] U. Lindstrom, “Supersymmetry, a Biased Review”, **arXiv:hep-th/0204016v2**, (2002).

[23] L. Bergstrom *et al*, “Observability of Gamma Rays from Dark Matter Neutralino Annihilations in the Milky Way Halo”, *Astropart. Phys*, **9**, 137-162, (1998).

[24] J. Angle *et al*, “First Results from the XENON10 Dark Matter Experiment at the Gran Sasso National Laboratory”, *Astrophysical Journal*, **arXiv:0706.0039v1**, (2007).

[25] E. Aprile *et al*, “Simultaneous Measurement of Ionization and Scintillation from Nuclear Recoils in Liquid Xenon for a Dark Matter Experiment”, *Physical Review Letters*, **97**, 081302, (2006).

[26] Glenn F. Knoll, “Radiation Detection and Measurement”, *Wiley*, New York, (2000).

[27] SAES Getters, *http://www.puregastechnologies.com*, (2007).

[28] E. Aprile *et al*, “Observation of Anticorrelation Between Scintillation and Ionization for MeV Gamma Rays in Liquid Xenon”, *Physical Review B (Condensed Matter and Materials Physics)*, **76**, 014115, (2007).

[29] D. S. Akerib *et al*, “Deep Underground Science and Engineering Lab: S1 Dark Matter Working Group”, **arXiv.org:astro-ph/0605719**, (2006).

[30] E. Aprile *et al*, “Scintillation Response of Liquid Xenon to Low Energy Nuclear Recoils”, *Physical Review D (Particles and Fields)*, **72**, 072006, (2005).

[31] E. Aprile *et al*, “Detection of Gamma-Rays with a 3.5 l Liquid Xenon Ionization Chamber Triggered by the Primary Scintillation Light”, *Nucl. Inst. Meth. A*, **480**, 636, (2002).

[32] E. Aprile *et al*, “A Liquid Xenon Time Projection Chamber for Gamma-Ray Imaging in Astrophysics: Present Status and Future Directions”, *Nucl. Inst. Meth. A*, **461**, 256, (2001).

[33] S. Asztalos *et al*, "Experimental Constraints on the Axion Dark Matter Halo Density", *Astrophysical Journal*, **571**, L27, (2002).

[34] P. Belli *et al*, "Effect of the Galactic Halo Modeling on the DAMA-NaI Annual Modulation Result: An Extended Analysis of the Data for Weakly Interacting Massive Particles with a Purely Spin-Independent Coupling", *Phys. Rev. D*, **66**, 043503, (2002).

[35] Andreas Birkedal-Hansen and Jay G. Wacker, "Scalar Dark Matter from Theory Space", *Physical Review D (Particles, Fields, Gravitation, and Cosmology)*, **69**, 065022, (2004).

[36] R. Catena *et al*, "Dark Matter Relic Abundance and Scalar-Tensor Dark Energy", *Physical Review D (Particles, Fields, Gravitation, and Cosmology)*, **70**, 063519, (2004).

[37] R. Abusaidi *et al*, "Exclusion Limits on the WIMP-Nucleon Cross Section from the Cryogenic Dark Matter Search", *Phys. Rev. Lett.*, **84**, 5699-5703, (2000).

[38] K. Ni, "Development of a Liquid Xenon Time Projection Chamber for the XENON Dark Matter Search", Columbia University PhD Thesis, (2006).

[39] M. Yamashita, "Dark Matter Search Experiment with Double Phase Xe Detector", Waseda University PhD Thesis, Japan, (2003).

[40] J. D. Vergados, "Theoretical Directional and Modulated Rates for Direct Supersymmetric Dark Matter Detection", *Phys. Rev. D*, **67**, 103003, (2003).

[41] T. Takahashi *et al*, "Average Energy Expended per Ion Pair in Liquid Xenon", *Phys. Rev. A*, **12**, 1771-1775, (1975).

[42] G.M. Seidel *et al*, "Rayleigh Scattering in Rare-Gas Liquids", *Nucl. Inst. Meth. A*, **489**, 189-194, (2002).

[43] R. D. Peccei *et al*, "CP Conservation in the Presence of Pseudoparticles", *Phys. Rev. Lett.*, **38**, 1440-1443, (1977).

BIOGRAPHICAL SKETCH

Jesse Angle was born in 1980 in Seattle, Washington. He and his family lived in the Puget Sound area for all of his formative years. Graduating from Sumner High School in 1998, Jesse went on to receive the bachelor of science degree in both physics and astronomy from the University of Washington in Seattle. On completing his undergraduate studies, Jesse moved to Florida to study graduate physics at the University of Florida in Gainesville.

During the course of his studies he earned a master's degree in physics and married his wonderful wife, Wendi Angle. His graduate studies were made more complicated with the birth of his twin sons, Kasimir and Lucian. Nearing the end of his graduate work, Jesse and Wendi welcomed their third son, Aurelius, to the family. After completing his doctorate, Jesse intends to continue researching astronomy and astrophysics, possibly also applying his skills to teach the next generation.